Chapter 2
Single Band Effective Mass Equation and Envolvent Functions

Abstract The single-band effective mass Schrödinger equation to calculate the envelope functions is described and its grounds are shown. These envelope functions are used to multiply periodic part of the Bloch functions to obtain approximate eigenfunctions of the Hamiltonian of a nanostructured semiconductor. The Bloch functions, which are the product of a periodic function and a plane wave, constitute the exact solution of a homogeneous semiconductor; they are taken as a basis to represent the nanostructured Hamiltonian. The conditions that make possible the use of this single band effective mass Schrödinger equation are explained. The method is applied to the calculation of the energy spectrum of quantum dots for wavefunctions belonging to the conduction band. A box-shaped model of the quantum dots is adopted for this task. The results show the existence of energy levels detached from this band as well as eigenfunctions bound totally or partially around the quantum dot. The absorption coefficients of photons in the nanostructured semiconductor, which is our ultimate goal, are calculated. The case of spherical quantum dots is also considered.

The easiest way to approach to the behavior of electrons in semiconductors is the use of effective mass equations. This is presented in this chapter for the specific cases of nanostructured semiconductors. The approximate treatment presented here applies to the case that the nanostructure has a mesoscopic size, much larger than the size of the semiconductor microscopic structure, that is, where the individual atoms are located.

We shall see that the effective mass equation is only of application when we are dealing with electrons in a single semiconductor band, namely the conduction band. Therefore, the bipolar behavior, crucial for the understanding of most semiconductor devices, in which both electrons and holes enter into the game—or in other words, when electrons in the CB and in the VB are to be considered—cannot be explained with the resources of the simple effective mass treatment studied in this chapter. They will be properly studied in the following chapter. Nevertheless, the

detailed study of the simple effective mass equation, besides its intrinsic interest, is a needed step towards the study in the following chapter.

Furthermore, in nanostructured materials, another crucial concept arises which is that of envelope functions. This concept is studied in this chapter for the first time in this book, although it will also be the subject of other chapters for more complicated cases.

2.1 Quantum Mechanical Grounds

We present in this section the quantum mechanical grounds that lead to the use of the effective mass equation and also the envelope functions. This section is mainly inspired in Datta [1, Chap. 6], whose full reading is recommended.

As we have indicated, the nanostructures studied here are of mesoscopic size, in that their dimensions are much larger than the interatomic spacing of their constituent semiconductors. Because of this, we present first the integral factorization rule that will be used in approximate calculations along this book.

2.1.1 The Integral Factorization Rule

Let us consider first that $f(\boldsymbol{r})$ is a slowly varying function (it is assumed to vary in the mesoscopic range) and $g(\boldsymbol{r})$ is periodic with the short period of the crystalline unit cell $\Omega_{cell,0}$ (the crystal is a repetition of this cell) of volume Ω_{cell}. Ω is the full crystal volume. $\Omega_{cell,\boldsymbol{n}}$ is the cell $\boldsymbol{n}$ with origin in $\boldsymbol{r}_{\boldsymbol{n}}$.

The integral factorization rule states that,[1]

$$\int_{\Omega} f(\boldsymbol{r})g(\boldsymbol{r})d^3r \cong \left(\int_{\Omega} f(\boldsymbol{r})d^3r \right) \left(\int_{\Omega_{cell}} g(\boldsymbol{r})\frac{d^3r}{\Omega_{cell}} \right) \tag{2.1}$$

To prove this, let us first accept that, for any function that varies slowly within the unit cells, as is the case of $f(\boldsymbol{r})$,

$$\sum_{\boldsymbol{n}} \Omega_{cell}f(\boldsymbol{r}_{\boldsymbol{n}}) \cong \int_{\Omega} f(\boldsymbol{r})d^3r \tag{2.2}$$

---

[1] The division by Ω_{cell} is necessary, among other reasons, to keep the dimensionality.

and then let us consider evident that for any function $h(\boldsymbol{r})$,

$$\int\limits_{\Omega_{cell,n}} h(\boldsymbol{r})d^3r = \int\limits_{\Omega_{cell,0}} h(\boldsymbol{r}+\boldsymbol{r_n})d^3r \qquad (2.3)$$

Taking this into account, we can write

$$\int\limits_{\Omega} f(\boldsymbol{r})g(\boldsymbol{r})d^3r = \sum_n \int\limits_{\Omega_{cell,n}} f(\boldsymbol{r})g(\boldsymbol{r})d^3r = \sum_n \int\limits_{\Omega_{cell,0}} f(\boldsymbol{r}+\boldsymbol{r_n})g(\boldsymbol{r}+\boldsymbol{r_n})d^3r \quad (2.4)$$

Defining $\Delta_n(\boldsymbol{r}) = f(\boldsymbol{r}+\boldsymbol{r_n}) - f(\boldsymbol{r_n})$ and taking also into account the periodicity of $g(\boldsymbol{r})$,

$$\int\limits_{\Omega} f(\boldsymbol{r})g(\boldsymbol{r})d^3r = \left(\int\limits_{\Omega_{cell,0}} g(\boldsymbol{r})\frac{d^3r}{\Omega_{cell}}\right)\sum_n f(\boldsymbol{r_n})\Omega_{cell} + \sum_n \Omega_{cell}\int\limits_{\Omega_{cell,0}} \Delta_n(\boldsymbol{r})g(\boldsymbol{r})\frac{d^3r}{\Omega_{cell}}$$

$$\cong \left(\int\limits_{\Omega} f(\boldsymbol{r})d^3r\right)\left(\int\limits_{\Omega_{cell,0}} g(\boldsymbol{r})\frac{d^3r}{\Omega_{cell}}\right) + \int\limits_{\Omega}\left(\int\limits_{\Omega_{cell,0}} \Delta_n(\boldsymbol{r})g(\boldsymbol{r})\frac{d^3r}{\Omega_{cell}}\right)d^3r$$

$$\qquad (2.5)$$

Since our assumption is that the variation of $f(\boldsymbol{r_n})$ in the $\Omega_{cell,0}$ cell is negligible and therefore $\Delta_n(\boldsymbol{r})$ is also negligible, the last term of the second line expression is negligible so that Eq. (2.1) is proven.

A second order approximation may help us to keep a clear idea of the approximation involved in using Eq. (2.1). Let us further consider the last term in Eq. (2.5). For this, let us develop $\Delta_n(\boldsymbol{r})$ in series around the origin to the first order,

$$\Delta_n(\boldsymbol{r}) = f(\boldsymbol{r}+\boldsymbol{r_n}) - f(\boldsymbol{r_n}) \cong \nabla f(\boldsymbol{r_n}) \cdot \boldsymbol{r} \qquad (2.6)$$

where $\nabla f(\boldsymbol{r_n})$ are the gradients of $f(\boldsymbol{r_n})$ calculated at specific points $\boldsymbol{r_n}$; this forms a set of constant vectors,

$$\sum_n \Omega_{cell}\int\limits_{\Omega_{cell,0}} \Delta_n(\boldsymbol{r})g(\boldsymbol{r})\frac{d^3r}{\Omega_{cell}} \cong \sum_n \Delta\Omega_{cell}\nabla f(\boldsymbol{r_n}) \cdot \left(\int\limits_{\Omega_{cell,0}} \boldsymbol{r}g(\boldsymbol{r})\frac{d^3r}{\Omega_{cell}}\right) \qquad (2.7)$$

Assuming that $\nabla f(\boldsymbol{r_n})$ varies slowly in each unit cells so allowing us to apply Eq. (2.2), we can write, in a second order approximation,

$$\int\limits_{\Omega} f(\boldsymbol{r})g(\boldsymbol{r})d^3r \cong \left(\int\limits_{\Omega} f(\boldsymbol{r})d^3r\right)\left(\int\limits_{\Omega_{cell,0}} g(\boldsymbol{r})\frac{d^3r}{\Omega_{cell}}\right) + \left(\int\limits_{\Omega} \nabla f(\boldsymbol{r_n})d^3r\right)$$
$$\cdot\left(\int\limits_{\Omega_{cell,0}} \boldsymbol{r}g(\boldsymbol{r})\frac{d^3r}{\Delta\Omega_{cell}}\right) \tag{2.8}$$

In this equation the last term is small mainly because r, when restricted to the unit cell at the origin, is small. For further discussion: it will be common that $\int_{\Omega} f(\boldsymbol{r})d^3r$ is normalized to one. If $f(\boldsymbol{r})$ is not zero in a radius R its height in this region will be of the order of $3/4\pi R^3$ (in a region comprising many unit cells), its derivative will be of the order of $3/4\pi R^4$ and $\int_{\Omega} \nabla f(\boldsymbol{r_n})d^3r$ will be of the order of $1/R$. On the other hand, it will be also common that $\int_{\Omega_{cell,0}} g(\boldsymbol{r})d^3r/\Omega_{cell}$ will also be one and $\int_{\Omega_{cell,0}} rg(\boldsymbol{r})d^3r/\Omega_{cell} = r_{incell}$ with r_{incell} a value smaller than the unit cell average radius. In consequence the last term of Eq. (2.8) is of the order of r_{incell}/R, which is assumed to be small. Of course this is a rough calculation that has to be taken with care. For more accuracy, the value of the last term as compared with the first term (equal to one for the normalized functions) clarifies the accuracy of the approximation.

2.1.2 The Envelope Equation in a Nanostructured Semiconductor

Let $\Xi(\boldsymbol{r}, t)$ be a solution of the time-independent Schrödinger equation (TISE)

$$(H + U)\Xi(\boldsymbol{r}) = E\Xi(\boldsymbol{r}) \tag{2.9}$$

where

$$H = -(\hbar^2/2m_0)\nabla^2 + U_L(\boldsymbol{r}) \tag{2.10}$$

$U_L(\boldsymbol{r})$ being a periodic lattice potential and $U = U(\boldsymbol{r})$ a mesoscopically varying potential,[2] for instance, in the space charge region of a junction. It is well know that, in a homogeneous semiconductor, the eigenfunctions $H|v, \boldsymbol{k}\rangle = E_v(\boldsymbol{k})|v, \boldsymbol{k}\rangle$ are the Bloch functions. In $E_v(\boldsymbol{k})$, $\boldsymbol{k}$ can be considered any vector of the reciprocal space within the 1st Brillouin zone or, more often, any of the nodes of a lattice when the

---

[2] Note that, in the non-relativistic limit, the energies in the Schrödinger equations do not have a defined energy origin. However, the origin for E and U_L have to be the same and U must be considered as a potential energy that is added to U_L.

configuration space is limited to a finite, although large, volume Ω. Therefore, we may also write $E_v(\mathbf{k}) = E_{v,\mathbf{k}}$.

The *energy dispersion* $E_v(\mathbf{k})$ is a function known for many semiconductors, at least in the region of the $\mathbf{k}$-space where it is of interest. In many cases it is taken as parabolic. In this chapter,

$$E_v(\mathbf{k}) = E_{v,0} + \hbar^2 k^2 / 2m^* \tag{2.11}$$

with m^* being the effective mass and $E_{v,0}$ the extremum, or edge, of the band v, for instance the CB bottom. The effective mass m^* is approximately isotropic for zincblende semiconductors although it is direction-dependent for some other semiconductors. Note that Eq. (2.11) is a second order development of $E_v(\mathbf{k})$ and $E_v(0) = E_{v,0}$ is an extremum (maximum or minimum). In general, $E_v(\mathbf{k})$ can be more complex and may admit a development in series of (k_x, k_y, k_z) that, in any case, has to be symmetric with respect to the origin [2]. In nanostructured semiconductors, $E_{v,0}$ vary spatially with the nanostructure, forming an additional mesoscopic potential that, as we shall see, for all practical effects may be added to the mesoscopic potential U, the latter often being zero. It has to be born in mind that the Bloch function solutions are strictly valid only in homogeneous semiconductors; the validity of a dependence on $\mathbf{r}$ in $E_v(\mathbf{k})$ has to be taken with caution.

The Bloch functions are[3]

$$|v, \mathbf{k}\rangle \equiv u_{v,\mathbf{k}}(\mathbf{r})\frac{e^{i\mathbf{k}\cdot\mathbf{r}}}{\sqrt{\Omega}}; \quad \langle v', \mathbf{k}' \mid v, \mathbf{k}\rangle \equiv \int_\Omega u^*_{v',\mathbf{k}'}u_{v,\mathbf{k}}e^{i(\mathbf{k}-\mathbf{k}')\cdot\mathbf{r}}\frac{d^3\mathbf{r}}{\Omega} = \delta_{v,v'}\delta_{\mathbf{k},\mathbf{k}'} \tag{2.12}$$

($\equiv$ means equal by definition) with $u_{v,\mathbf{k}}(\mathbf{r})$ a function with the translational symmetry of the lattice. When $\mathbf{k} = \mathbf{k}'$, the orthonormality condition becomes

$$\int_\Omega u^*_{v',\mathbf{k}}u_{v,\mathbf{k}}\frac{d^3r}{\Omega} = \delta_{v,v'} = \frac{N_{cells}}{\Omega}\int_{\Omega_{cell}} u^*_{v',\mathbf{k}}u_{v,\mathbf{k}}d^3r = \int_{\Omega_{cell}} u^*_{v',\mathbf{k}}u_{v,\mathbf{k}}\frac{d^3r}{\Omega_{cell}} \tag{2.13}$$

where N_{cells} is the number of unit cells in the crystal. This gives an orthonormalization rule (similar to the one in Sect. 2.1.1) for the periodic part of the Bloch functions; the normalization of the $u_{v,\mathbf{k}}$ functions is obtained by average-normalizing them to one in a single unit cell. The orthogonality is always fulfilled.

We want to prove that the full wavefunction, $\Xi(\mathbf{r}, t)$, can be approximately expressed as the product of a periodic function (the periodic part of a Bloch function), $u_{v,0}(\mathbf{r})$, and an *envolent, $\Phi(\mathbf{r}, t)$*, that is,

$$\Xi(\mathbf{r}, t) \cong u_{v,0}(\mathbf{r})\Phi(\mathbf{r}, t) \tag{2.14}$$

---

[3] Some authors, and more frequently those working in the k·p method, call Bloch functions to their periodic part, $u_{v,\mathbf{k}}(\mathbf{r})$.

where the *envolvent* fulfils the effective mass equation, defined as

$$(E_v(-i\nabla) + U)\Phi(\boldsymbol{r}, t) = E\Phi(\boldsymbol{r}, t) \tag{2.15}$$

$(E_v(-i\nabla)$ is $E_v(\boldsymbol{k})$ where $\boldsymbol{k} \to -i\nabla)$ under certain conditions to be discussed later. Strictly speaking, the transformation rule $E_v(-i\nabla) \to E_v(\boldsymbol{k})$ is a consequence of the Fourier transforms and is not straightforwardly valid if $E_v(\boldsymbol{k})$ also depends on $\boldsymbol{r}$. In this book we usually ignore this difficulty.

It will be proven later that, in the specific case of $E(\boldsymbol{k})$ given by Eq. (2.11), the effective mass equation is

$$-\frac{\hbar^2}{2m^*}\nabla^2\Phi + (E_{v,0} + U)\Phi = E\Phi \tag{2.16}$$

Even in a homogeneous material, the periodic part of the Bloch functions is not easily known. There are approximations, and group theory provides some properties of these functions, but in most cases the used properties are the result of an indirect measurement. In some cases, in particular in the so called *ab initio* quantum calculations, they are theoretically obtained, but this implies a heavy calculation burden and, ultimately, the accuracy of these calculations is to be tested against measurements.

As already mentioned, $E_{v,0}$ depends on the position; it is different in the nanostructure than in the host semiconductor, leading to a mesoscopic quasi-potential, different in each band. The same can be said of the effective mass m^*; however, its variation makes uncertain the application of the rule $\boldsymbol{k} \to -i\nabla$ and may lead to the adoption of a non-Hermitical kinetic energy operator (see e.g. [1, p. 191]). We shall come later again to this point. In this work, we shall consider m^* constant throughout the whole nanostructured semiconductor. Since in the bound states the envelope functions are concentrated in the nanostructure, the m^* adopted is the one corresponding to the nanostructure, whose material becomes, in this way, the *semiconductor of reference*; however, the adoption of the host material m^* should be better for extended envelope functions.

Even neglecting the dependence of m^* on the position due to the nanostructure, Eq. (2.11) has a dependence on $\boldsymbol{k}$ but also, through $E_{v,0}$, on $\boldsymbol{r}$. This will be taken into account in the proof to follow.

2.1.3 Proof of the Effective Mass Equation for Obtaining the Envolvent

The proof goes along the following path: first, using the Bloch functions of the homogeneous semiconductors of reference as a basis, we obtain a given solution of the nanostructure. It is found that, when the periodic part of the Bloch function of a band does not sensibly vary with $\boldsymbol{k}$ in the range of small $\boldsymbol{k}$s, the wavefunction for

this band becomes decoupled from the other bands. Then, coefficients of the Bloch function development of the nanostructure solution obtained in this case are found to be the same as the ones resulting from solving the effective mass equation with a development of plane waves. This straightforwardly provides a proof of Eq. (2.14).

Let us start by developing $\Xi(\mathbf{r})$ in the basis of Bloch functions of the semiconductor of reference.

$$\Xi(\mathbf{r}) = \sum_{v,\mathbf{k}} \varphi_{v,\mathbf{k}} |v, \mathbf{k}\rangle \tag{2.17}$$

The coefficients of the Bloch functions may be obtained from the TISE (Eq. (2.9)) through a set of linear equations in the variables $\varphi_{v,\mathbf{k}}$. For this, we use Eq. (2.17) and the dispersion function of Eq. (2.11),

$$\sum_{v,\mathbf{k}} E_{v,0} \phi_{v,\mathbf{k}} |v, \mathbf{k}\rangle + \sum_{v,\mathbf{k}} \frac{\hbar^2 k^2}{2m^*} \phi_{v,\mathbf{k}} |v, \mathbf{k}\rangle + \sum_{v,\mathbf{k}} U \phi_{v,\mathbf{k}} |v, \mathbf{k}\rangle = E \sum_{v,\mathbf{k}} \phi_{v,\mathbf{k}} |v, \mathbf{k}\rangle \tag{2.18}$$

After putting primes in the indices of Eq. (2.18), this equation is left-multiplied by $\langle v, \mathbf{k}|$; with some rearrangement of terms, we obtain.

$$\left(\frac{\hbar^2 k^2}{2m^*} - E \right) \phi_{v,\mathbf{k}} + \sum_{v',\mathbf{k}'} \langle v, \mathbf{k}|E_{v',0} + U|v', \mathbf{k}'\rangle \phi_{v',\mathbf{k}'} = 0 \tag{2.19}$$

$E_{v,0} + U$ depends on the space coordinates; however, they are contained in matrix elements that involve an integration whose result depends only on $(\mathbf{k}, \mathbf{k}')$ couples of permitted points in the Brillouin zone. For each band and each permitted value of $\mathbf{k}$ an equation is formed and the solution of the system of equations in Eq. (2.19) allows the calculation of all the $\phi_{v,\mathbf{k}}$ values. Note that the procedure is rigorous and the band edge position dependence has been grouped with the slow varying potential U. A position dependence of the effective mass is more difficult to treat.

Let us analyze the matrix elements. For this we take into account that $E_{v,0} + U$ are slowly varying functions and we assume, for the moment, that the only matrix elements of interest are those of small $\mathbf{k}$, so that $\exp[i(\mathbf{k} - \mathbf{k}') \cdot \mathbf{r}]$ are slow-varying functions. The integral factorization rule of Eq. (2.1) can then be applied and we also assume that, at least for a certain range, $u_{b,\mathbf{k}}(\mathbf{r})$ is independent of $\mathbf{k}$ in this small range of interest and therefore equal to $u_{b,\mathbf{k}'}(\mathbf{r})$. Using also the orthonormalization rule in Eq. (2.13), we can write

$$\langle b, \mathbf{k}|E_{v',0} + U|v', \mathbf{k}'\rangle \cong \int_\Omega (E_{v',0} + U)\mathrm{e}^{i(\mathbf{k}'-\mathbf{k})\cdot\mathbf{r}} \frac{d^3r}{\Omega} \int_{\Omega cell} u_{b,\mathbf{k}'}^* u_{v',\mathbf{k}'} \frac{d^3r}{\Omega_{cell}}$$
$$= \langle \mathbf{k}'|E_{b,0} + U|\mathbf{k}\rangle \delta_{b,v'} \tag{2.20}$$

where $|\mathbf{k}\rangle$ represents the plane wave

$$|\mathbf{k}\rangle \equiv \frac{e^{i\mathbf{k}\cdot\mathbf{r}}}{\sqrt{\Omega}} \tag{2.21}$$

Using Eq. (2.20), Eq. (2.19) will be written as

$$\left(\frac{\hbar^2 k^2}{2m^*} - E\right)\phi_{b,\mathbf{k}} + \sum_{\mathbf{k'}} \langle \mathbf{k}|E_{b,0} + U|\mathbf{k'}\rangle \phi_{b,\mathbf{k'}} = 0 \tag{2.22}$$

The condition for this to happen is that $u_{b,\mathbf{k}}(\mathbf{r})$ be independent of $\mathbf{k}$. Note that now this equation, corresponding to band b, is decoupled of all the other bands.

Let us now develop the effective mass Eq. (2.16) in plane waves

$$\Phi(\mathbf{r}) = \sum_{\mathbf{k}} \phi_{\mathbf{k}}|\mathbf{k}\rangle \tag{2.23}$$

(note that $|v,\mathbf{k}\rangle = u_{v,\mathbf{k}}(\mathbf{r})|\mathbf{k}\rangle$). This development is nothing more than the three-dimensional Fourier transform of $\Phi(\mathbf{r})$.

Substituting Eq. (2.23) into the effective mass Eq. (2.16) for the band b we obtain

$$\sum_{\mathbf{k}} \phi_{\mathbf{k}} \frac{\hbar^2 k^2}{2m^*}|\mathbf{k}\rangle + \sum_{\mathbf{k}} \phi_{\mathbf{k}}(E_{b,0} + U)|\mathbf{k}\rangle = E\sum_{\mathbf{k}} \phi_{\mathbf{k}}|\mathbf{k}\rangle \tag{2.24}$$

After putting primes on the indices of Eq. (2.24), this equation is left-multiplied by $\langle \mathbf{k}|$; with some rearrangement of terms, we obtain

$$\left(\frac{\hbar^2 k^2}{2m^*} - E\right)\phi_{\mathbf{k}} + \sum_{\mathbf{k'}} \langle \mathbf{k}|E_{b,0} + U|\mathbf{k'}\rangle \phi_{\mathbf{k'}} = 0 \tag{2.25}$$

This equation replicates Eq. (2.22) by taking $\phi_{\mathbf{k}} = \phi_{b,\mathbf{k}}$ for the given band b. Taking into account the plane wave development in Eq. (2.23), for a solution in the band b, Eq. (2.17) becomes,

$$\Xi(\mathbf{r}) = \sum_{\mathbf{k}} \phi_{\mathbf{k}}|\mathbf{k}\rangle u_{b,0}(\mathbf{r}) = \Phi(\mathbf{r})u_{b,0}(\mathbf{r}) \tag{2.26}$$

So demonstrating Eq. (2.14) and proving that $\Phi(\mathbf{r})$ is a solution of the effective mass Eq. (2.16), with the parameters (effective mass and band-edge profile) of the band b.

Some of the assumptions may be tested now. Since $E_{v,0} + U$ varies slowly because of its big size compared to the lattice constant, for large values of $\mathbf{k} - \mathbf{k'}$,

$$\langle \boldsymbol{k}|U + E_{v,0}|\boldsymbol{k}'\rangle = \int_{\Omega} (E_{v,0} + U)e^{i(k-k')\cdot r}\frac{d^3\boldsymbol{r}}{\Omega} \cong 0 \qquad (2.27)$$

This implies that, for large values of $\boldsymbol{k}$, $(E_{v,\boldsymbol{k}} - E)\phi_{\boldsymbol{k}}(t) \cong 0$ and $\phi_{\boldsymbol{k}}(t) \cong 0$. Actually, this is a well known property of the Fourier transform: extended $\boldsymbol{r}$-functions have a localized $\boldsymbol{k}$-Fourier transform. This confirms that the large values of $\boldsymbol{k}$ lack interest in the context of the problem examined here.

The constant character of $u_{v,\boldsymbol{k}}$ in the restricted domain of useful $\boldsymbol{k}$s is not to be taken for granted. In practice, the one-band approximation will be reasonable for the CB of most semiconductors with zincblende structure, but it is not a general property. For cases in which this condition cannot be assumed, multiple-band effective mass equations have been developed, as is studied later in this book.

2.1.4 Elements of Matrix for the Intraband Absorption

The IB $\rightarrow$ CB absorption, that for reasons to be seen later, is called intraband absorption, is proportional to the dipole [3, 4] element of matrix $|\langle \Xi'|\boldsymbol{\varepsilon} \cdot \boldsymbol{r}|\Xi\rangle|^2$, where the two wavefunctions describe two different states (at least one of them bound around the nanostructure). In this equation, $\boldsymbol{\varepsilon}$ is the polarization vector of the incident photon. The full expression for the absorption coefficient will be explained in Sect. 2.4.

Using Eq. (2.14) and applying the Integral Factorization Rule of Eq. (2.1) we can write

$$|\langle \Xi'|\boldsymbol{\varepsilon} \cdot \boldsymbol{r}|\Xi\rangle|^2 = \left|\langle u_{v,0}\Phi'|\boldsymbol{\varepsilon} \cdot \boldsymbol{r}|u_{v,0}\Phi\rangle\right|^2 = \left|\int_{\Omega cell} u_{v,0}^* u_{v,0}\frac{d^3r}{\Omega_{cell}}\int_{\Omega} \Phi'^* \boldsymbol{\varepsilon} \cdot \boldsymbol{r}\Phi d^3r\right|^2$$

$$= \left|\int_{\Omega} \Phi'^* \boldsymbol{\varepsilon} \cdot \boldsymbol{r}\Phi d^3r\right|^2 \qquad (2.28)$$

Therefore, the intraband absorption calculations, when at least one wavefunctions is bound, can be performed by using just the envelope functions and disregarding the periodic part of the Bloch functions.

When the two states in the transition are extended along the whole semiconductor, the element of matrix used here is not valid [5]. Another element of matrix is then to be used, as explained in Chap. 5 of this book.

2.1.5 The Variable-Effective-Mass Envelope Hamiltonian

We assume Eq. (2.11) to be the position dependent dispersion equation for a nanostructured material, and use the Bloch functions of a certain reference homogeneous semiconductor as a basis.

As before, let us now develop $\Xi(\boldsymbol{r})$ in the basis of the Bloch functions of Eq. (2.17). The coefficients of the Bloch functions (corresponding to a discrete set of values of $\boldsymbol{k}$ in the first Brillouin zone) may be obtained from the TISE Eq. (2.9) through a set of linear equations in the variables $\phi_{v,k}$. We substitute Eqs. (2.11) and (2.17) in Eq. (2.9)

$$\sum_{v,k} \phi_{v,k} E_{v,0}(\boldsymbol{r})|v,\boldsymbol{k}\rangle + \sum_{v,k} \phi_{v,k} \frac{\hbar^2 k^2}{2m^*(\boldsymbol{r})}|v,\boldsymbol{k}\rangle + \sum_{v,k} \phi_{v,k} U(\boldsymbol{r})|v,\boldsymbol{k}\rangle = E \sum_{v,k} \phi_{v,k}|v,\boldsymbol{k}\rangle \tag{2.29}$$

and, multiplying on the left by $\langle b,\boldsymbol{k}|$ (after having put primes to all the running indices), we obtain the desired system of equations

$$-E\phi_{b,k} + \sum_{v',k'} \phi_{v',k'} \langle b,\boldsymbol{k}|E_{v',0}(\boldsymbol{r}) + \frac{\hbar^2 k'^2}{2m^*(\boldsymbol{r})} + U(\boldsymbol{r})|v',\boldsymbol{k}'\rangle = 0 \tag{2.30}$$

All the dependence on $\boldsymbol{r}$ is in the second term sum. However, it is contained in matrix elements that involve an integration whose result depends only on $(\boldsymbol{k},\boldsymbol{k}')$ couples of permitted points in the Brillouin zone. For each band and each permitted value of $\boldsymbol{k}$, an equation is formed and the solution of the system of equations in Eq. (2.30) allows the calculation of all the $\phi_{v,k}$ values.

Notice that we have left-multiplied by the bra state $\langle b,\boldsymbol{k}|$ corresponding to the band in which $u_{b,k}(\boldsymbol{r})$ is independent of $\boldsymbol{k}$. Therefore, with the same arguments used in the discussion of Eq. (2.20), we can now write

$$\langle b,\boldsymbol{k}|E_{v',0}(\boldsymbol{r}) + \frac{\hbar^2 k'^2}{2m^*(\boldsymbol{r})} + U(\boldsymbol{r})|v',\boldsymbol{k}'\rangle$$
$$\cong \int_\Omega (E_{v',0}(\boldsymbol{r}) + \frac{\hbar^2 k'^2}{2m^*(\boldsymbol{r})} + U)e^{i(\boldsymbol{k}'-\boldsymbol{k})\cdot\boldsymbol{r}} \frac{d^3 r}{\Omega} \int_{\Omega cell} u_{b,k'}^* u_{v',k'} \frac{d^3 r}{\Omega_{cell}}$$
$$= \langle \boldsymbol{k}'|E_{b,0} + \frac{\hbar^2 k'^2}{2m^*(\boldsymbol{r})} + U|\boldsymbol{k}\rangle \delta_{b,v'} \tag{2.31}$$

So that the equation referring to band b,

$$-E\phi_{b,k} + \sum_{k'} \phi_{b,k'} \langle b,\boldsymbol{k}|E_{b,0}(\boldsymbol{r}) + U(\boldsymbol{r})|b,\boldsymbol{k}'\rangle + \sum_{k'} \phi_{b,k'} \langle b,\boldsymbol{k}| \frac{\hbar^2 k'^2}{2m^*(\boldsymbol{r})}|b,\boldsymbol{k}'\rangle = 0 \tag{2.32}$$

has been decoupled from all the terms belonging to other bands. The last sum we have separated from the preceding one will deserve our attention.

Let us look for a suitable effective mass equation. The application of the transformation rule $\boldsymbol{k} \to -i\nabla$ will lead to the following effective mass equation[4]

$$i\nabla\left(\frac{\hbar^2}{2m^*(\boldsymbol{r})}\right)i\nabla\Phi + \left(E_{b,0}(\boldsymbol{r}) + U(\boldsymbol{r})\right)\Phi = E\Phi \tag{2.33}$$

where, in the position-dependent term containing $\boldsymbol{k}^2$, this transformation has been made according to the rule $\boldsymbol{k}^2 f(\boldsymbol{r}) \to i\nabla f(\boldsymbol{r})i\nabla$ for any real function $f(\boldsymbol{r})$ of $\boldsymbol{r}$. This is necessary because the operator resulting from a straightforward application of the rule $\boldsymbol{k} \to -i\nabla$ is not Hermitical (see for instance [3, Chap. VII] or [1, Chap. 6]).

Let us now develop this equation in basis of plane waves. By following the same steps used to get Eq. (2.25) we obtain

$$-E\phi_{\boldsymbol{b}}(E) + \sum_{\boldsymbol{k}'} \phi_{\boldsymbol{k}'} \langle \boldsymbol{b}|E_{b,0}(\boldsymbol{r}) + U(\boldsymbol{r})|\boldsymbol{k}'\rangle + \sum_{\boldsymbol{k}'} \phi_{\boldsymbol{k}'} \langle \boldsymbol{b}|\frac{\hbar^2 \boldsymbol{k}\boldsymbol{k}'}{2m^*(\boldsymbol{r})}|\boldsymbol{k}'\rangle = 0 \tag{2.34}$$

We can see that the last term of this equation differs somewhat from the last term of Eq. (2.32). This difference disappears if $m^*(\boldsymbol{r})$ is constant; in this case both equations become

$$-E\phi_{b,\boldsymbol{k}} + \sum_{\boldsymbol{k}'} \phi_{b,\boldsymbol{k}'} \langle b,\boldsymbol{k}|E_{b,0}(\boldsymbol{r}) + U(\boldsymbol{r})|b,\boldsymbol{k}'\rangle + \phi_{b,\boldsymbol{k}}\frac{\hbar^2 k^2}{2m^*} = 0 \tag{2.35}$$

which is the same as Eq. (2.22).

Thus we may conclude that the effective mass Eq. (2.33) sometimes proposed [6] to represent nanostructured semiconductors is not exactly the same as the one obtained when accepting the dispersion Eq. (2.11) when we accept that the effective mass is position dependent.

To avoid the conflict we use in this book a position independent effective mass in the way discussed before.

2.2 Box Shaped Quantum Dots

As described in the Introduction chapter, the confined levels associated with quantum dots (QDs) have been used to form a suitable IB. As represented in Fig. 2.1, large spacers have been used, of about 80 nm, between the layers of QDs,

---

[4] In this equation, the imaginary unit i is conserved attached to the gradient sign ∇. This is because $i\nabla$ is Hermitical. The advantage of using Hermitical operators is that $\langle\varphi|i\nabla|\psi\rangle = \int \varphi^* i\nabla\psi d^3 r = \int (i\nabla\varphi)^*\psi d^3 r$.

QD-IBSC structure
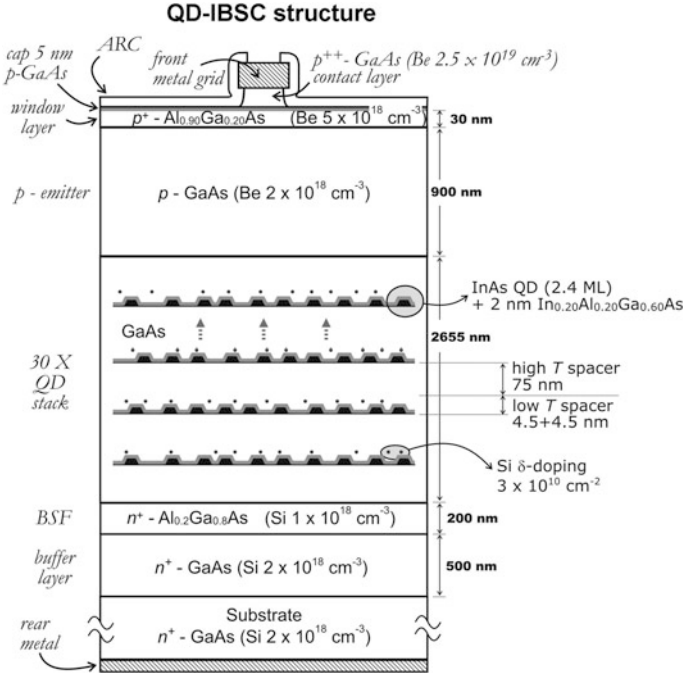
Fig. 2.1 Schematic of the solar cells used for the Isc-Voc measurements in Fig. 1.3. Reproduced with permission. © 2012, Elsevier [9]

instead of the more frequently used ones of about 20 nm, to avoid tunneling between QDs and permit the CB quasi-Fermi level to go beyond the IB levels [7] (only at low temperature) so permitting higher voltages. Indeed the big spacers decrease the volume density of QDs. These are actually only necessary in the edge of the QD region, where an electric field is produced to form the built-in potential. This involves six or seven QD layers near the p region. The use of field damping layers [8] is one proposed solution, and has been successfully used to avoid this drawback. However, it has not been used in the cell modeled in this chapter.

In particular, most of the calculations concerning the QD-IBSC along this chapter correspond to the sample SB of Ref. [7] (which is similar but not the same as that in Fig. 2.1). This is called the SOTA (state of the art) prototype in this book. Data for the calculations along the book are in Table 2.1.

2.2.1 Eigenvalues and Eigenfunctions in the Separation of Variables Approximation

The shape of the QDs is a matter of controversy and, as shown in this chapter, this shape has an important influence on their behavior. The most common understanding

Table 2.1 Parameters and dimensions used in the SOTA prototype

	Parameter	Symbol	Units	Value
QD (InAs)	Conduction band effective mass	m_{cb}/m_0		0.0294
	Light holes effective mass	m_{lh}/m_0		0.027
	Heavy holes effective mass	m_{hh}/m_0		0.333
	Split-off holes effective mass	m_{so}/m_0		0.076
	Conduction band offset	U_{cb}	eV	0.473
	Valence band offset for lh and hh	U_{vb}	eV	0.210
	Band offset for the split-off holes	U_{so}		0.341
	Index of refractions	n_{ref}		3.5
Barrier (GaAs)	Conduction band effective mass	m_{cb}/m_0		0.0613
	Barrier material bandgap (300 K)	E_g	eV	1.42
Dimensions	QD height	$2c$	nm	6
	QD base side	$2a = 2b$	nm	16
Array	Coverage factor of the QDs	F_s		0.1024
	QD layers density	N_l	cm^{-1}	125,000

of the InAs QD grown on (1,0,0) GaAs is that they are squat truncated pyramids of quadrangular base. Different authors have adopted different shapes in their calculations, with the probable motivation of fitting the shape to their models. In particular, spherical shape [11, 12], lens shape [13] or box shape [14, 15] have been selected. We also adopt the box shape, as seen in the lower part of Fig. 2.2, with dimensions $2a \times 2a \times 2c$.

The effective mass Eq. (2.16) can be written as

$$\frac{\hbar^2}{2m^*} \frac{\nabla^2 \Phi}{\Phi} + E = U(\boldsymbol{r}) \tag{2.36}$$

where the right-hand-side term is the band-edge position that that in the rest of this part will be denoted as $U(\boldsymbol{r})$ instead of $(E_{b,0} + U)$, despite the fact that $E_{b,0}(\boldsymbol{r})$, that in most cases will be $E_C(\boldsymbol{r})$, is the only non-null term of $(E_{b,0} + U)$. The energy origin is arbitrary and, for the calculations, the zero is set at the bottom of the potential well inside the QD (i.e. at the dot material conduction-band edge) and V outside it. In symbolic language ($\forall$ = for all, $\wedge$ = and, $\vee$ = or),

$$U(\boldsymbol{r}) = \begin{cases} 0 & \forall |x| < a \wedge |y| < a \wedge |z| < c \\ V & \forall |x| \geq a \vee |y| \geq a \vee |z| \geq c \end{cases} \tag{2.37}$$

However, for presentation purposes, the zero shall be set at the barrier material conduction band edge, which means that V must be subtracted from all the energy results.
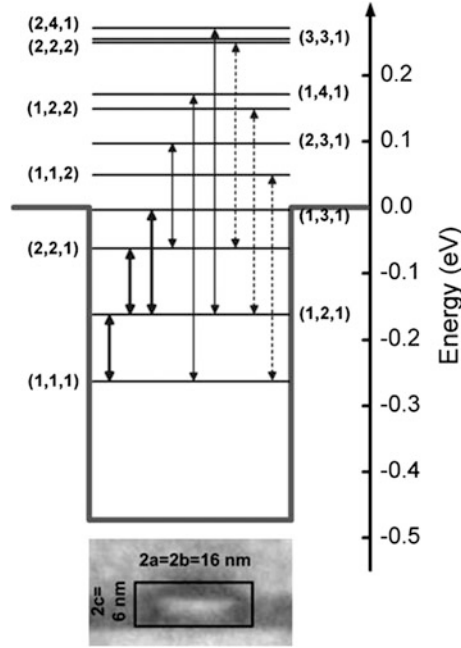
Fig. 2.2 Potential well and separation-of-variables energy levels in a box shaped potential well with the dimensions shown in the figure. *Solid arrows* are permitted transitions under vertical or isotropic illumination; *dotted* are permitted under isotropic illumination only. *Thicker lines* show the main electron flow. Levels (121) collect the electrons received directly from the VB and via the levels (111) and (221) (the latter going downwards) and send them to the (131) level. *Below* TEM photograph of a QD showing its dimensions. Reproduced with permission. © 2011, the authors [10]

2.2.1.1 One-Dimensional Solutions

The functions $\xi(x)$, $\psi(y)$, $\zeta(z)$ are defined by

$$\frac{\hbar^2}{2m^*}\frac{d^2\xi/dx^2}{\xi} + E_x = \begin{cases} 0 & \forall\, |x| < a \\ V & \forall\, |x| \geq a \end{cases} \tag{2.38}$$

and similarly for $\psi(y)$, $\zeta(z)$ (in the latter case using c instead of a as the well boundary).

Finding the solutions for $\xi(x)$ (or for $\psi(y)$, $\zeta(z)$) constitutes a simple exercise of differential equations. In this context, a discussion is provided e.g. in [16]. For $E < V$ (the subindex x is dropped in this subsection) bounded solutions, different from the trivial $\xi(x) \equiv 0$, are even $(\cos(kx))$ or odd $(\sin(kx))$ harmonic functions inside the well, flanked by fading exponential functions outside it $(\exp(-\kappa x)\ \forall\, x \geq a)$. The wavefunctions must be normalizable in an infinite space, and, as such, non-fading exponential functions outside the QD are unphysical. The energy E, fading coefficient κ and k-values are related by

$$E = \hbar^2 k^2/2m^* = V - \hbar^2\kappa^2/2m^* \tag{2.39}$$

The condition for cancellation of the non fading solutions is that the logarithmic derivative of the harmonic solution inside the QW must be matched to the logarithmic derivative of the fading solution outside it, that is,

$$\cot(k_n a) = k_n/\kappa_x = k_n a \bigg/ \sqrt{\varpi^2 a^2 - k_n^2 a^2} \quad \text{for even functions}$$

$$-\tan(k_n a) = k_n/\kappa_x = k_n a \bigg/ \sqrt{\varpi^2 a^2 - k_n^2 a^2} \quad \text{for odd functions} \tag{2.40}$$

$$\sqrt{\frac{2m^* V}{\hbar^2}} \equiv \varpi$$

The functions to the right and the left of the equalities above are represented in Fig. 2.3. The index n—a quantum number (QN)—denotes the different permitted energies in increasing order. Odd QNs correspond to even functions and vice versa.

Note that the rightmost side expression has a vertical asymptote at $ka = \varpi a$. There are positive branches of the minus-tangent and cotangent functions every $\pi/2$. Therefore, the number of confined states is the number of times $\pi/2$ is contained in ϖa plus one. The only parameter in the equations above is ϖa, or, in other words, $m^* V a^2$. This means that the number of confined states depends strongly on the size of the QD and, to a lesser extent, on the confining potential V and on the effective mass. The dependence on V and $m*$ is of the same importance, such that doubling the effective mass and halving the potential leaves the root unchanged, although this will also have the effect of halving the energies of the levels, as seen in Eq. (2.39). However, increasing the size while keeping the effective mass and potential unchanged increases greatly the number of confined states, as is visible by comparing plots (a) and (b) of Fig. 2.3.

Table 2.2 presents the values of k for the different QNs and the one-dimensional energy. The CB offset and QD dimensions are those in [17] and are derived from
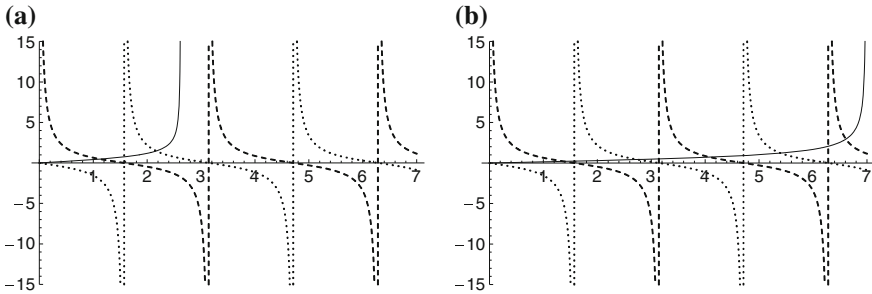
Fig. 2.3 The two members of the equations $\cot(k_n a) = k_n a/\sqrt{\varpi^2 a^2 - k_n^2 a^2}$ and $-\tan(k_n a) = k_n a/\sqrt{\varpi^2 a^2 - k_n^2 a^2}$ versus $k_n a$ for U = 0.473 eV, m = 0.0294 times the electron mass; **a** a = 3nm and **b** b = 8 nm. *Dashed curve* (cot) for even and *dotted* (−tan) for odd states. Second term of the equality, *solid line*

Table 2.2 Values of k (multiplied by the potential well half-width) and one-dimensional energy for the CB offset and QD dimensions in [17]. Energies are with respect to the QD material CB bottom

x-,y-eigenfunctions					z-eigenfunctions	
n	1	2	3	4	1	2
$k_x a$, $k_z c$	1.299	2.579	3.806	4.810	0.992	1.775
E_0 (eV)	0.034	0.135	0.292	0.469	0.142	0.453

$U = 0.473$ eV; $m^* = 0.0294\ m_0$; $a = b = 8$ nm; $c = 3$ nm

the data of the SOTA prototype (different of those in Fig. 2.3). We have used the InAs effective mass because the bound functions mainly span this material.

For $E \geq V$, the solution is harmonic with wavenumber k inside the potential well and also harmonic, even or odd, outside it but with a different value of the wavenumber k_e and a phase term. That is, they are of the form $\cos(k_e x - \theta)$ or $\sin(k_e x - \theta)$. Details can be found, e.g. in [17]. In this case,

$$E = V + \hbar^2 k_e^2/2m^* = \hbar^2 k^2/2m^* \qquad (2.41)$$

and

$$\begin{aligned}
(k_e/k)\cot(ka) &= \cot(k_e a - \theta) \\
(k_e/k)\tan(ka) &= \tan(k_e a - \theta)
\end{aligned} \qquad (2.42)$$

respectively for the even and odd functions.

For $E \geq V$, k_e can take any value and therefore it leads to a continuum spectrum of energies. Since the mathematics of continuum spectra is rather complicated, it is common to assume that the wavefunctions are restricted to a large but finite region (a segment of length $2L$, with large L, for one-dimensional cases, or a big parallelepiped for three-dimensional ones) and assume periodic conditions there. This leads [17] to

$$k_e L - \theta = \tilde{n}\pi/2 \qquad (2.43)$$

where $\tilde{n}$ is an integer, odd for the even solutions and even for the odd solutions.

Due to the hermitical property of the Hamiltonian, any two eigenfunctions, bound or extended, are strictly orthogonal. For easier handling, the eigenfunctions must be normalized. This is easy for bound functions (it may be calculated analytically). Strictly speaking, extended states cannot be normalized (at least in the ordinary sense) but this difficulty is circumvented by integrating the square of the eigenfunction's absolute value in the interval $(-L, +L)$. If outside the QD the harmonic function has amplitude one, this integration is approximately L (and the wavefunction norm is $L^{1/2}$) if L is much larger than the QD dimensions. L it is arbitrarily chosen but any measurable magnitude has, under this model, an expression containing L that cancels out the L dependence.

2.2.1.2 Three-Dimensional Solutions

By adding the one-dimensional Eq. (2.38) corresponding to the three coordinates we obtain

$$\frac{\hbar^2}{2m^*} \frac{\nabla^2 \Phi}{\Phi} + E_{0,n_x,n_y,n_z} = U_0(\mathbf{r}) \tag{2.44}$$

where

$$\begin{aligned}
\Phi(x,y,z) &= \xi(x)\psi(y)\zeta(z) \\
E_{0,n_x,n_y,n_z} &= E_{x,n_x} + E_{y,n_y} + E_{z,n_z}
\end{aligned} \tag{2.45}$$

However, $U_0(\mathbf{r})$ is different from $U(\mathbf{r})$. As explained in [16, 18], it is the same inside the QD and outside it in front of the faces, but it takes the value $2V$ in front of the edges and of $3V$ in front of the corners. In symbolic language,

$$U_0(\mathbf{r}) = \begin{cases}
0 & \forall\, |x|<a \wedge |y|<a \wedge |z|<c \\
V & \forall\, |x| \geq a \wedge |y|<a \wedge |z|<c \\
V & \forall\, |x|<a \wedge |y| \geq a \wedge |z|<c \\
V & \forall\, |x|<a \wedge |y|<a \wedge |z| \geq c \\
2V & \forall\, |x| \geq a \wedge |y| \geq a \wedge |z|<c \\
2V & \forall\, |x| \geq a \wedge |y|<a \wedge |z| \geq c \\
2V & \forall\, |x|<a \wedge |y| \geq a \wedge |z| \geq c \\
3V & \forall\, |x| \geq a \wedge |y| \geq a \wedge |z| \geq c
\end{cases} \tag{2.46}$$

Thus, the Hamiltonian we want to solve can be written as

$$H = -\frac{\hbar^2}{2m^*} \nabla^2 + U_0(\mathbf{r}) + U'(\mathbf{r}) = H_0 + U'(\mathbf{r}) \tag{2.47}$$

where the perturbation potential is

$$U'(\mathbf{r}) = U(\mathbf{r}) - U_0(\mathbf{r}) = \begin{cases}
0 & \forall\, |x|<a \wedge |y|<a \wedge |z|<c \\
0 & \forall\, |x| \geq a \wedge |y|<a \wedge |z|<c \\
0 & \forall\, |x|<a \wedge |y| \geq a \wedge |z|<c \\
0 & \forall\, |x|<a \wedge |y|<a \wedge |z| \geq c \\
-V & \forall\, |x| \geq a \wedge |y| \geq a \wedge |z|<c \\
-V & \forall\, |x| \geq a \wedge |y|<a \wedge |z| \geq c \\
-V & \forall\, |x|<a \wedge |y| \geq a \wedge |z| \geq c \\
-2V & \forall\, |x| \geq a \wedge |y| \geq a \wedge |z| \geq c
\end{cases} \tag{2.48}$$

(notice that here we have defined H as the effective mass Hamiltonian for the envolvent equation; in Sect. 2.1, H represented the lattice one-electron Hamiltonian). This perturbation is spatially limited to the corners and edges of the QD and is zero in

the rest of the space. The separation-of-variables model assumes it is negligible. The separation-of-variables eigenfunctions can be labeled through three QNs: $|n_x, n_y, n_z\rangle = \xi_{n_x} \psi_{n_y} \zeta_{n_z} = \Phi_{n_x, n_y, n_z}$. They are the eigenfunctions of the Hamiltonian H_0. Each one-dimensional eigenfunction may be bound or extended. To distinguish this fact we can write $|\hat{n}_x, \tilde{n}_y, \hat{n}_z\rangle$ where $\hat{n}_x$ indicates that the x-eigenfunction is bound and $\tilde{n}_y$ denotes that the y-eigenfunction is extended. The H_0 eigenvalues are in Eq. (2.45) whose components may be found in Eqs. (2.39) or (2.41). As said before, we usually subtract V from the values obtained to refer the energies to the barrier material CB bottom.

While in one dimension, the bound states (BSs) energy was always below the potential well rim, this is not true in three-dimensional BSs, as shown in Fig. 2.2. These states have been considered by several researchers [19, 20], and sometimes are interpreted as resonances between plane waves; often they are called virtual bound states (VBSs). Their interpretation in the effective mass Hamiltonian equation is straightforward.

The set $|n_x, n_y, n_z\rangle$ (this notation is equivalent to (n_x, n_y, n_z)) forms an orthonormal basis that, nevertheless, is somewhat involved. It is formed of purely bound states $|\hat{n}_x, \hat{n}_y, \hat{n}_z\rangle$ (0E states), of purely extended states $|\tilde{n}_x, \tilde{n}_y, \tilde{n}_z\rangle$ (3E states) and of states that are mixed, with a single extended state, of the type $|\hat{n}_x, \hat{n}_y, \tilde{n}_z\rangle$ (and all the circular permutations: 1Ez, 1Ex, 1Ey states) and with a two extended states $|\tilde{n}_x, \tilde{n}_y, \hat{n}_z\rangle$ (and all the circular permutations: 2Exy, 2Eyz, 2Ezx states). The QN corresponding to the extended states is linked, as indicated in Eq. (2.43) to a certain value of L and it may be physically more meaningful to use k_e and the parity as the wavefunction definer, although, for calculations, we shall use the corresponding QN (the closest one of the same parity, once L is given). The relationship between the description based on QNs and k_e and parity are given by Eqs. (2.43) and (2.42).

Examples of H_0 eigenfunctions of the 0E, 1E and 2E sets are given in Fig. 2.4.

If H_0 is developed in this basis, it forms a diagonal matrix, although the ordering of the diagonal elements in this matrix is complicated. For instance we can start by
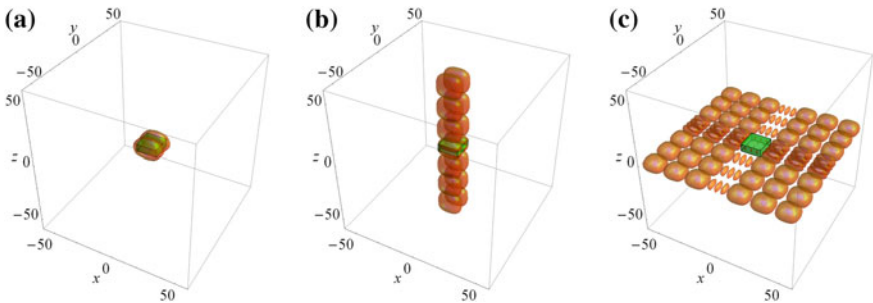
Fig. 2.4 Electron probability density contours. **a** Bound 0E (1,2,1) wavefunction; **b** filamentary 1Ez (1,2,8) wavefunction; **c** sheet-shaped 2Exy (5,8,1) wavefunction. Space units are in nm; the containing cube length is $2L = 120$ nm. SOTA prototype; the parallelepipedic box (in *green*, online) represents the QD, of $16 \times 16 \times 6$ nm^3. The contour drawn corresponds to 0.001 times the maximum probability density of the (1,1,1) 0E state. Reproduced with permission. © 2013, Elsevier [18]

ordering the finite number of states of the bound 0E states and then put the 3E states, but they are infinite, and we still have to situate the 2E and 1E states.

Note that, for extended states, the electron tends to be outside the QD. It might be reasonable that we use the GaAs effective mass for these states. However, this might compromise the orthogonality of these states with the bound states. Maybe in a problem not dealing with bound states at all it might be better to use the GaAs effective mass. Another option is to use the so called Bastard boundary conditions to be examined next.

2.2.2 Separation of Variables with Position-Dependent Effective Mass

This case has been discussed in Sect. 2.1.5 and it has been rejected for the mainstream of this book. Nevertheless the discussion is completed in this subsection.

The effective mass equation is

$$i\nabla\left(\frac{\hbar^2}{2m^*(\boldsymbol{r})}\right)i\nabla\Phi + \left(E_{b,0}(\boldsymbol{r}) + U(\boldsymbol{r})\right)\Phi = E\Phi \tag{2.49}$$

For the region inside the QD the effective mass is constant and the variable effective mass Eq. (2.33) is identical to the one for constant effective mass Eq. (2.16); therefore the solutions are the same. The same can be said of the regions outside the QD and in front of the QD box faces, although, in this case, the effective mass is that of the barrier material and not that of the QD. The difference arrives at the interfaces. There, the one dimensional equation is

$$-\frac{d}{dx}\left(\frac{\hbar^2}{2m^*(x)}\right)\frac{d\xi(x)}{dx} + U(x)\xi(x) = E_x\xi(x) \tag{2.50}$$
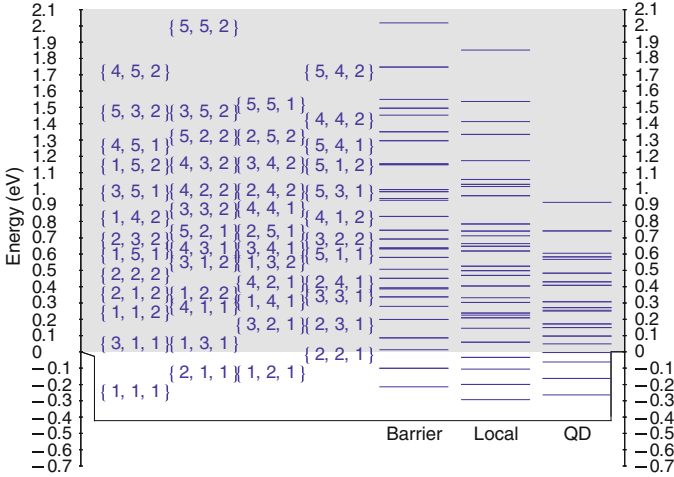
By integrating this equation at the two sides of one interface,

$$-\left(\frac{\hbar^2}{2m^*(x)}\right)\frac{d\xi(x)}{dx}\bigg|_{a-\varepsilon}^{a+\varepsilon} = \int_{a-\varepsilon}^{a+\varepsilon}(E_x - U(x))\xi(x)dx \cong 0$$

$$\text{or} \tag{2.51}$$

$$\left(\frac{\hbar^2}{2m^*_{GaAs}}\right)\frac{d\xi(a+\varepsilon)}{dx} = \left(\frac{\hbar^2}{2m^*_{InAs}}\right)\frac{d\xi(a-\varepsilon)}{dx}$$

In summary, the quantity to be matched at the interface is the derivative of the wavefunction divided by the effective mass. This conditions is often called Bastard

Fig. 2.5 Energy spectrum of the box shaped QD of the SOTA cell, using the barrier material effective mass (label barrier), the variable effective mass case (label local) and the QD effective mass (label QD). The QNs refer only to the barrier case

boundary condition [6]. It differs to the case of a spatially constant effective mass, for which just the derivative of the wavefunction must be matched.

Figure 2.5 presents the position of the fully confined energy levels for the SOTA cell when taking the barrier material effective mass (GaAs, $0.0613m_0$), the QD effective mass (InAs, $0.0294m_0$) and the variation contemplated in this subsection. It is interesting to observe the big difference between selecting the barrier material effective mass, which we estimated best for the study of extended wavefunctions, and the QD effective mass, which we considered best for confined states. The variable-effective-mass solution resembles the latter case for low energy and the former for high energy states. It must be pointed out that the variable effective mass presents a lower energy in the fundamental state than the case with the QD effective mass.

As we have discussed in Sect. 2.1.5, the variable-effective-mass approach does not clearly justify eigenfunctions which are the product of an envolvent times the periodic part of a Bloch function. Nonetheless, if we accept the position-variable dispersion Eq. (2.11), their spectrum is close to the two spectra we recommend for bound and extended functions, with the QD and barrier effective mass respectively. Given the Hermitical nature of the operator in Eq. (2.50), its eigenvalues are orthogonal. Therefore, the variable-effective-mass wavefunctions are a good practical choice for many problems. Nevertheless, we do not use them further in this book.

It is clear that also in this case the separation of variables, treated above, is only an approximation. In the edge and corner regions the solutions found do not fulfill the differential Eq. (2.33), for reasons associated to the variable effective mass, which are additional to those already discussed in Sect. 2.2.1.

2.3 Exact Resolution of the Mass Effective Equation with a Potential Box-Shaped Well

As discussed in Sect. 2.2.1.1, the separation-of-variables method produces an inexact solution to the differential Eq. (2.33). In this section, Eq. (2.33) is solved exactly, without using a separation of variables. The resulting exact Hamiltonian is going to be represented as a matrix in a basis of separation-of-variables wavefunctions, here called the standard basis, and then diagonalized. It closely follows Ref. [18], whose reading is recommended for further understanding.

2.3.1 Integration in Regions

As derived from the perturbation potential in Eq. (2.48), the matrix elements of the perturbation Hamiltonian $\langle n_{x,1}, n_{y,1}, n_{z,1} | U'(\boldsymbol{r}) | n_{x,2}, n_{y,2}, n_{z,2} \rangle$ require the integrations of wavefunctions restricted to a certain region of the space, multiplied by a multiple of V. This section is devoted to the calculation of these integrals.

The complex conjugation necessary in quantum mechanics for the internal products and matrix elements is not used here because all the functions are real.

In Tables 2.3 and 2.4, the values of the integral inside and outside the QD are presented for bound one-dimensional eigenfunctions in the x and z coordinates respectively. The column to the left represents the internal product; for different QNs it must be zero. The very small values observed in some cases are to be considered the noise background of our calculations. For small QNs, the probability of finding the electron outside the QD (look at the cases with equal QNs) is very small, so justifying the choice of the QD effective mass. For large QNs it may be more spread out. When the parity of the QNs is different, the product of wavefunctions is odd and its integral is zero inside the QD. Outside it, it takes different signs for positive and negative abscissas. When the QNs are different, but of the same parity, the integrals inside and outside the QD balance out.

For extended one-dimensional eigenfunctions of different QNs, the orthogonality is theoretically required and well verified in our calculations. Thus, for $L \to \infty$ (the amplitude of $\xi_{\tilde{n}_x}$ is rendered zero by the normalization),

$$\int\limits_{-a}^{a} \xi_{\tilde{n}_x} \xi_{\tilde{n}_x'} dx = 0$$

$$\int\limits_{-\infty}^{-a} \xi_{\tilde{n}_x} \xi_{\tilde{n}_x'} dx + \int\limits_{a}^{\infty} \xi_{\tilde{n}_x} \xi_{\tilde{n}_x'} dx = \delta_{\tilde{n}_x, \tilde{n}_x'} \tag{2.52}$$

and for bound/extended eigenfunctions

Table 2.3 Integration in regions of bound one-dimensional eigenfunctions corresponding to the coordinates x or y

QNs	$\int_{-\infty}^{\infty} \xi_{\hat{n}_x} \xi_{\hat{n}'_x} dx$	$\int_{-\infty}^{a} \xi_{\hat{n}_x} \xi_{\hat{n}'_x} dx$	$\int_{-a}^{a} \xi_{\hat{n}_x} \xi_{\hat{n}'_x} dx$	$\int_{a}^{\infty} \xi_{\hat{n}_x} \xi_{\hat{n}'_x} dx$
1,1	1	0.00638387	0.987232	0.00638387
1,2	0	0.0133362	0	-0.0133362
1,3	1.606×10^{-16}	-0.0217575	0.0435151	-0.0217575
1,4	0	-0.0267906	0	0.0267906
2,2	1	0.0279778	0.944044	0.0279778
2,3	0	-0.0461097	0	0.0461097
2,4	-3.47531×10^{-17}	-0.059098	0.118196	-0.059098
3,3	1	0.0779097	0.844181	0.0779097
3,4	0	0.111237	0	-0.111237
4,4	1	0.336536	0.326929	0.336536

Table 2.4 Integration in regions of bound one-dimensional eigenfunctions corresponding to the coordinate z

QNs	$\int_{-\infty}^{\infty} \zeta_{\hat{n}_z} \zeta_{\hat{n}'_z} dz$	$\int_{-\infty}^{c} \zeta_{\hat{n}_z} \zeta_{\hat{n}'_z} dz$	$\int_{-c}^{c} \zeta_{\hat{n}_z} \zeta_{\hat{n}'_z} dz$	$\int_{c}^{\infty} \zeta_{\hat{n}_z} \zeta_{\hat{n}'_z} dz$
1,1	1	0.000375021	0.99925	0.000375021
1,2	0	0.00328518	0	-0.00328518
2,2	1	0.0345654	0.930869	0.0345654

$$\int_{-a}^{a} \xi_{\hat{n}_x} \xi_{\tilde{n}_x} dx = 0$$
$$\int_{-\infty}^{-a} \xi_{\hat{n}_x} \xi_{\tilde{n}_x} dx + \int_{a}^{\infty} \xi_{\hat{n}_x} \xi_{\tilde{n}_x} dx = 0 \tag{2.53}$$

The y- and z-eigenfunctions behave similarly.

2.3.2 The Exact Hamiltonian Matrix Elements, Eigenvalues and Eigenvectors

The exact Hamiltonian matrix, when developed in eigenfunctions of the Hamiltonian H_0 of Eq. (2.27), is the sum of the matrix representation of H_0, which is a diagonal matrix, and the matrix representation of U', described in Eq. (2.48).

The matrix elements of the latter are

$$\langle n_x, n_y, n_z | U' | n'_x, n'_y, n'_z \rangle$$

$$= -V \left[\int\limits_{-a}^{a} \xi_{n_x} \xi_{n'_x} dx \left(\int\limits_{-\infty}^{-a} \psi_{n_y} \psi_{n'_y} dy + \int\limits_{a}^{\infty} \psi_{n_y} \psi_{n'_y} dy \right) \left(\int\limits_{-\infty}^{-c} \zeta_{n_z} \zeta_{n'_z} dz + \int\limits_{c}^{\infty} \zeta_{n_z} \zeta_{n'_z} dz \right) \right.$$

$$+ \left(\int\limits_{-\infty}^{-a} \xi_{n_x} \xi_{n'_x} dx + \int\limits_{a}^{\infty} \xi_{n_x} \xi_{n'_x} dx \right) \int\limits_{-a}^{a} \psi_{n_y} \psi_{n'_y} dy \left(\int\limits_{-\infty}^{-c} \zeta_{n_z} \zeta_{n'_z} dz + \int\limits_{c}^{\infty} \zeta_{n_z} \zeta_{n'_z} dz \right)$$

$$+ \left(\int\limits_{-\infty}^{-a} \xi_{n_x} \xi_{n'_x} dx + \int\limits_{a}^{\infty} \xi_{n_x} \xi_{n'_x} dx \right) \left(\int\limits_{-\infty}^{-a} \psi_{n_y} \psi_{n'_y} dy + \int\limits_{a}^{\infty} \psi_{n_y} \psi_{n'_y} dy \right) \int\limits_{-c}^{c} \zeta_{n_z} \zeta_{n'_z} dz \right]$$

$$- 2V \left[\left(\int\limits_{-\infty}^{-a} \xi_{n_x} \xi_{n'_x} dx + \int\limits_{a}^{\infty} \xi_{n_x} \xi_{n'_x} dx \right) \left(\int\limits_{-\infty}^{-a} \psi_{n_y} \psi_{n'_y} dy + \int\limits_{a}^{\infty} \psi_{n_y} \psi_{n'_y} dy \right) \left(\int\limits_{-\infty}^{-c} \zeta_{n_z} \zeta_{n'_z} dz + \int\limits_{c}^{\infty} \zeta_{n_z} \zeta_{n'_z} dz \right) \right]$$

$$(2.54)$$

where no distinction has been made between bound and extended states.

According to Eq. (2.53), the matrix elements linking a bound and an extended wavefunction in a given coordinate are zero. Therefore, the only non-zero matrix elements are those belonging to the same set (0E, 3E etc.) of those enumerated in Sect. 2.2.1.2. This is the same as saying that the Hamiltonian matrix is the direct sum of the Hamiltonian matrices in these sets. In other words, it is a diagonal of blocs, although many of these blocs are of infinite dimension.

2.3.2.1 Purely Bound 0E States

For the sizes and potential of the SOTA cell there are 4 QNs for the x and y one-dimensional eigenfunctions and 2 for the z one-dimensional eigenfunction. Thus, there are 32 H_0 eigenfunctions for BSs and VBSs. The eigenvalues are calculated as a sum of the one-dimensional eigenvalues, as shown in Eq. (2.45) using Table 2.2 where these eigenvalues are given. They are represented in Fig. 2.6a. The energy first-order approximation (see for instance [3])

$$E_{1,n_x,n_y,n_z} = E_{0,n_x,n_y,n_z} + \langle n_x, n_y, n_z | U' | n_x, n_y, n_z \rangle \qquad (2.55)$$

is also presented there.

Notice that the first order approximation moves all the states downward. This shift is very little for the low energies but substantial for the high energies.

An exact calculation of the perturbed Hamiltonian, that is, the exact one within the model limitations, can be obtained by calculating the matrix
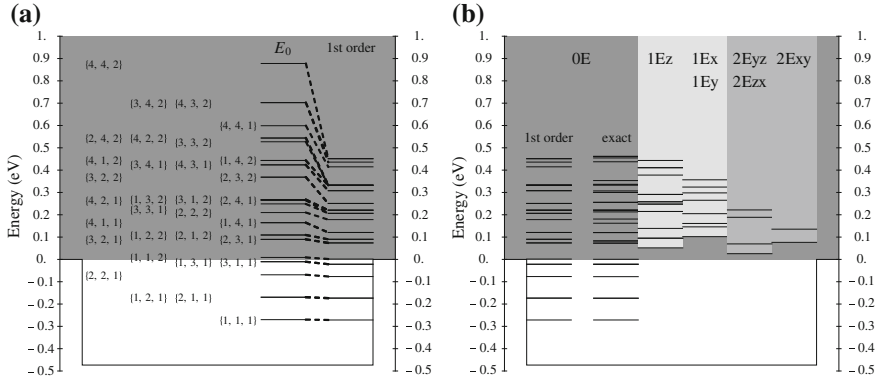
Fig. 2.6 **a** QD well and energy eigenvalues of $E_{0,nx,ny,nz}$ and their correction to the 1st order. The QNs corresponding to each energy line are also given. **b** Energy eigenvalues for the 1st order approximation, the same as in part (**a**), and from the exact calculations for the different sets of eigenfunctions. *Dark grey* corresponds to the energies of the continuum of 3E states. *Lighter* and *medium grey* correspond to the 1E and 2E states respectively, the *horizontal lines* show where the continuum spectrum starts above the energy of the bound part of the wavefunctions. One continuum of energies starts above each *horizontal line* in these two groups of sets. Reproduced with permission. © 2013, Elsevier [18]
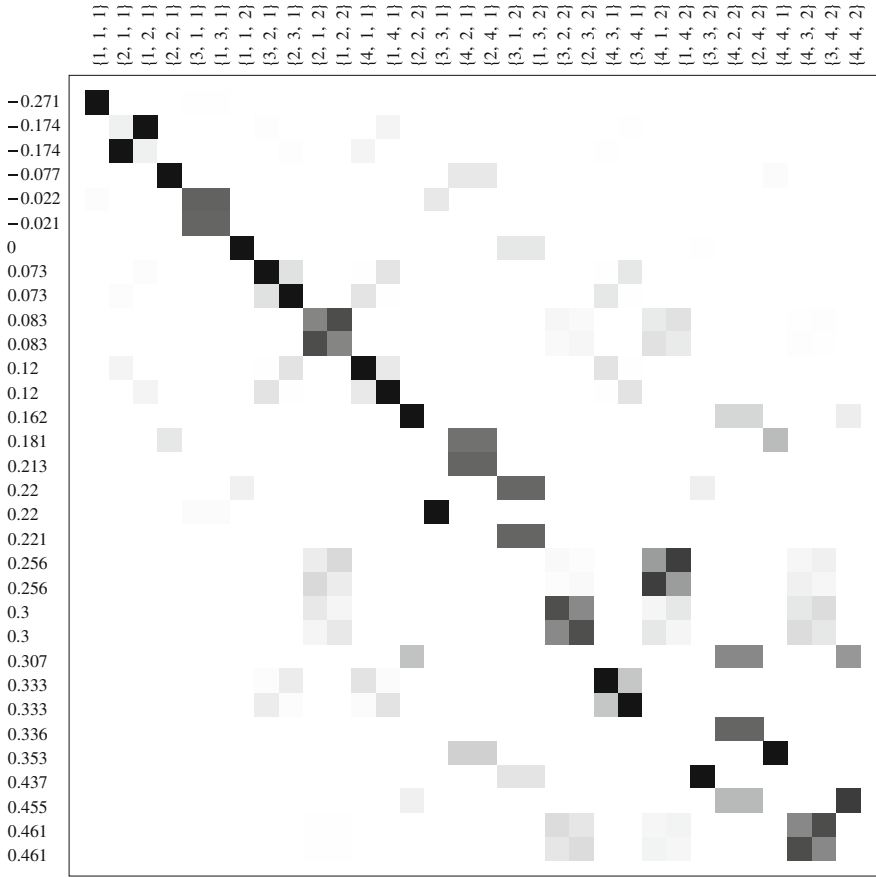
$$\langle n_x, n_y, n_z | H | n'_x, n'_y, n'_z \rangle = \langle n_x, n_y, n_z | H_0 | n'_x, n'_y, n'_z \rangle + \langle n_x, n_y, n_z | U' | n'_x, n'_y, n'_z \rangle$$

(2.56)

and obtaining the eigenvalues and eigenvectors. Of course, H_0, developed in the standard basis, is a diagonal matrix of elements equal to E_{0,n_x,n_y,n_z}. The eigenvalues are shown in Fig. 2.6b side by side with the 1st order approximations (which are also in part (a) of the figure) for easy comparison. Changes are small but visible for the high energies. It must be stressed that, for the exact calculations, the energy levels cannot be related to any set of QNs. In fact, the eigenstates are linear combinations of the unperturbed Hamiltonian eigenstates that are the product of one-dimensional wavefunctions, each with one QN. This relationship is represented in Fig. 2.7. The absolute value of the coefficient of $|n_x, n_y, n_z\rangle$ is represented in a gray scale (1 black; 0 white). The numeric values are given in the Supplemental Material of Ref. [18].

It can be seen that, in general, there are a small number of dominant unperturbed states corresponding to each exact state. Diagonal blocks of four boxes are often found sometimes corresponding to double degenerate states. The order of the unperturbed eigenstates on the top follows the order of the increasing E_{0,n_x,n_y,n_z} energies.

As an example, the bound states within the bandgap for the case in study (retaining only the terms producing a shadow in Fig. 2.7) are presented in Table 2.5.

Column labels (top, left to right): $|1,1,1\rangle$ $|2,1,1\rangle$ $|1,2,1\rangle$ $|2,2,1\rangle$ $|3,1,1\rangle$ $|1,3,1\rangle$ $|1,1,2\rangle$ $|3,2,1\rangle$ $|2,3,1\rangle$ $|2,1,2\rangle$ $|1,2,2\rangle$ $|4,1,1\rangle$ $|1,4,1\rangle$ $|2,2,2\rangle$ $|3,3,1\rangle$ $|4,2,1\rangle$ $|2,4,1\rangle$ $|3,1,2\rangle$ $|1,3,2\rangle$ $|3,2,2\rangle$ $|2,3,2\rangle$ $|4,3,1\rangle$ $|3,4,1\rangle$ $|4,1,2\rangle$ $|1,4,2\rangle$ $|3,3,2\rangle$ $|4,2,2\rangle$ $|2,4,2\rangle$ $|4,4,1\rangle$ $|4,3,2\rangle$ $|3,4,2\rangle$ $|4,4,2\rangle$

Row labels (left, in eV): -0.271, -0.174, -0.174, -0.077, -0.022, -0.021, 0, 0.073, 0.073, 0.083, 0.083, 0.12, 0.12, 0.162, 0.181, 0.213, 0.22, 0.22, 0.221, 0.256, 0.256, 0.3, 0.3, 0.307, 0.333, 0.333, 0.336, 0.353, 0.437, 0.455, 0.461, 0.461

Fig. 2.7 Strength of the projection of the eigenstates corresponding to the exact Hamiltonian eigenenergy, to the *left*, on the H_0 Hamiltonian eigenstates (*above*). *Black* full projection; *white* zero projection. Eigenstates are characterized by their energy (*left*, in eV). Reproduced with permission. © 2013, Elsevier [18]

Table 2.5 Exact eigenfunctions for the bound states within the bandgap

Eigenenergy (eV)	Eigenstate
-0.271	$1.000|1,1,1\rangle$
-0.174	$-0.083|2,1,1\rangle + 0.996|1,2,1\rangle - 0.015|3,2,1\rangle - 0.026|1,4,1\rangle$
-0.174	$0.996|2,1,1\rangle + 0.083|1,2,1\rangle - 0.015|2,3,1\rangle - 0.026|4,1,1\rangle$
-0.077	$-0.998|2,2,1\rangle + 0.038|4,2,1\rangle + 0.038|2,4,1\rangle$
-0.022	$0.016|1,1,1\rangle + 0.707|3,1,1\rangle + 0.707|1,3,1\rangle - 0.031|3,3,1\rangle$
-0.021	$-0.707|3,1,1\rangle + 0.707|1,3,1\rangle$
0.000	$-0.997|1,1,2\rangle + 0.056|3,1,2\rangle + 0.056|1,3,2\rangle$

Note that the probability of finding the electron in one of the term states is the square of the coefficient. For instance, the state in the second line of Table 2.5 is mainly $|1,2,1\rangle$. The probability of finding the electron in $|2,1,1\rangle$ is only 0.7 %.

In connection with the IBSC, the BS within the bandgap may be called IB states.

2.3.2.2 One-Dimensional Extended 1E States

This set is actually separated into three subsets, 1Ez, 1Ex and 1Ey, corresponding respectively to the states extended in z, x and y and bound in the remaining variables. Let us examine first the 1Ez states. The eigenvalues of H_0 are, according to Eqs. (2.46) and (2.41),

$$E_{0,n_x,n_y,k_{ez}} = E_{x,n_x} + E_{y,n_y} + \left(V + \hbar^2 k_{ez}^2/2m^*\right) - V \equiv E_{0,n_x,n_y,0} + \hbar^2 k_{ez}^2/2m^* \quad (2.57)$$

($\equiv$ involves a definition). Note that the energy in this equation is with respect to barrier material CB bottom; this results from subtracting V from the energies with respect to the QD CB bottom (the two Vs cancel). The second zero subindex in $E_{0,n_x,n_y,0}$ indicates that k_{ez} is zero.

The matrix elements now have two bound and one extended function; that is, using Eq. (2.52) they are

$$\langle \hat{n}_x, \hat{n}_y, \tilde{n}_z | U' | \hat{n}'_x, \hat{n}'_y, \tilde{n}'_z \rangle = \langle \hat{n}_x, \hat{n}_y | U' | \hat{n}'_x, \hat{n}'_y \rangle \delta_{\tilde{n}_z, \tilde{n}'_z}$$

where

$$\begin{aligned}
\langle \hat{n}_x, \hat{n}_y | U' | \hat{n}'_x, \hat{n}'_y \rangle \equiv -V \times \Bigg[&\int_{-a}^{a} \xi_{n_x} \xi_{n'_x} dx \left(\int_{-\infty}^{-a} \psi_{n_y} \psi_{n'_y} dy + \int_{a}^{\infty} \psi_{n_y} \psi_{n'_y} dy \right) \\
&+ \left(\int_{-\infty}^{-a} \xi_{n_x} \xi_{n'_x} dx + \int_{a}^{\infty} \xi_{n_x} \xi_{n'_x} dx \right) \int_{-a}^{a} \psi_{n_y} \psi_{n'_y} dy \Bigg] \\
- 2V \times \Bigg[&\left(\int_{-\infty}^{-a} \xi_{n_x} \xi_{n'_x} dx + \int_{a}^{\infty} \xi_{n_x} \xi_{n'_x} dx \right) \left(\int_{-\infty}^{-a} \psi_{n_y} \psi_{n'_y} dy + \int_{a}^{\infty} \psi_{n_y} \psi_{n'_y} dy \right) \Bigg]
\end{aligned}$$

$$(2.58)$$

This matrix is independent of k_{ez}, which appears in Eq. (2.57).

In this case, the exact Hamiltonian matrix is,

$$\langle \hat{n}_x, \hat{n}_y, \tilde{n}_z | H | \hat{n}'_x, \hat{n}'_y, \tilde{n}'_z \rangle = \left\{ \langle n_x, n_y | H_{0,0_z} | n'_x, n'_y \rangle + \langle n_x, n_y | U' | n'_x, n'_y \rangle + \hbar^2 k_{ez}^2/2m^* \right\} \delta_{\tilde{n}_z, \tilde{n}'_z}$$

$$(2.59)$$

where $H_{0,0_z}$ is the diagonal matrix of elements equal to $E_{0,n_x,n_y,0}$. In this equation, k_e is linked to $\tilde{n}_z$ by Eq. (2.43) where, for large values of $\tilde{n}_z$, θ may be neglected. Otherwise, Eq. (2.42) is to be used.

The eigenvalues of $H_{0,0_z} + U'$ are represented in Fig. 2.6b in the sector labeled 1Ez. In total, there are $4 \times 4 = 16$ states; many of them degenerate. According to Eq. (2.55), they are the threshold of sets of continuous states rising upwards. This is clearly represented for the lower energy state by a light gray rectangle, but it should be noted that a separate continuum emanates from each state in this plot sector.

The development of the 16 2-dimensional (2D) eigenfunctions on the 16 $|n_x, n_y\rangle$ states is presented in the Supplemental Material of Ref. [18]. The 3D eigenfunctions are in this case the product of the 2D eigenfunctions times the 1D extended (in/out phase harmonic) wave corresponding to k_{ez}.

The positions of the thresholds obtained from the exact solution are compared to those when the Hamiltonian is H_0 (separation-of-variables-solution) in the Supplemental Material of Ref. [18]. The thresholds for H_0 are actually located much further above those of the exact solution; the perturbation potential brings them down substantially. However, the exact-solution thresholds approach, but do not invade, the barrier material bandgap. The 1st order approximation gives closer values to the exact solution (see Supplemental Material of Ref. [18]), but in most cases not very close.

For the 1Ex and 1Ey sets, an analogous treatment is developed. In this case, there are $4 \times 2 = 8$ $|n_y, n_z\rangle$ states and the same for $|n_x, n_z\rangle$. They appear in Fig. 2.6b and are the thresholds of continuous spectra of states. The development of the 2-dimensional eigenstates in $|n_y, n_z\rangle$ and the $E_{0,0,n_y,n_z}$ and $E_{1,0,n_y,n_z}$ approximations or, for the $|n_x, n_z\rangle$ state, $E_{0,n_x,0,n_z}$ and $E_{1,n_x,0,n_z}$ approximations, can also be found in the Supplemental Material of Ref. [18]. The first-order approximations are obtained, similarly to in Eq. (2.55), by adding the diagonal element of U' to the zero-order approximation.

2.3.2.3 Two-Dimensional Extended 2E States

This subsection deals with three sets, 2Exy, 2Eyz and 2Ezx, corresponding respectively to bound states only in z, x and y and extended in the remaining variables. Let us examine first the 2Exy states. The eigenvalues of H_0 are

$$
\begin{aligned}
E_{0,k_{ex},k_{ey},n_z} &= E_{z,n_x} + \left(V + \hbar^2 k_{ex}^2/2m^*\right) + \left(V + \hbar^2 k_{ey}^2/2m^*\right) - V \\
&\equiv E_{0,0,0,n_z} + \hbar^2 k_{ex}^2/2m^* + \hbar^2 k_{ey}^2/2m^*
\end{aligned}
\tag{2.60}
$$

The subtracted V sets the energy origin at the barrier material CB bottom. The second and third zeroes in the subindex signify that k_{ex} and k_{ey} are zero.

The matrix elements now have one bound function and two extended; that is, they are, according to Eqs. (2.48) and (2.52),

$$\left\langle \tilde{n}_x, \tilde{n}_y, \hat{n}_z \middle| U' \middle| \tilde{n}'_x, \tilde{n}'_y, \hat{n}'_z \right\rangle = \left\langle \hat{n}_z \middle| U' \middle| \hat{n}'_z \right\rangle \delta_{\tilde{n}_x, \tilde{n}'_x} \delta_{\tilde{n}_y, \tilde{n}'_y}$$

where

$$\left\langle \hat{n}_z \middle| U' \middle| \hat{n}'_z \right\rangle \equiv -V\left[\int\limits_{-a}^{a} \zeta_{n_z}\zeta_{n'_z}dz\right] - 2V\left[\left(\int\limits_{-\infty}^{-a} \zeta_{n_z}\zeta_{n'_z}dx + \int\limits_{a}^{\infty} \zeta_{n_z}\zeta_{n'_z}dx\right)\right] \quad (2.61)$$

This matrix is independent of the k_es, which appears in Eq. (2.60).

With the exact model for 2Exy states, the Hamiltonian matrix development is

$$\left\langle \tilde{n}_x, \tilde{n}_y, \hat{n}_z \middle| H \middle| \tilde{n}'_x, \tilde{n}'_y, \hat{n}'_z \right\rangle = \left\{ \langle n_z | H_{0,0_x,0_y} | n'_z \rangle + \langle n_z | U' | n'_z \rangle \right.$$
$$\left. + \hbar^2 k_{ex}^2/2m^* + \hbar^2 k_{ey}^2/2m^* \right\} \delta(k_{ex}, k'_{ex})\delta(k_{ey}, k'_{ey}) \quad (2.62)$$

where $H_{0,0_x,0_y}$ is the diagonal matrix of elements of $E_{0,0,0,n_z}$. The eigenvalues of $H_{0,0_x,0_y} + U'$ are represented in Fig. 2.6b in the sector labeled 1Exy. For $|n_z\rangle$, there are only 2 states, which are the threshold of a set of continuous states rising upwards (medium gray rectangles). The development of the two 1D eigenfunctions on the two $|n_z\rangle$ states is presented in the Supplemental Material of Ref. [18]. The 3D eigenfunctions are in this case the product of the 1D eigenfunctions and two 1D extended (in/out phase harmonic) waves corresponding to the k_{ex} and k_{ey} vectors.

The same arguments may be applied to the 2Eyz and 2Ezx, where the bound states are $|n_x\rangle$ and $|n_y\rangle$ respectively. In this case, there are four states and four levels, which are represented in the corresponding sector of the Fig. 2.6b plot. Again the lowering of the $H_{0,0_y,0_z}$ or $H_{0,0_z,0_x}$ energy levels is very substantial, more than in the 1E sets; however, the levels do not penetrate into the bandgap, even though for the 2Eyz and 2Ezx sets they approach it closely. Details can be found in the Supplemental Material of Ref. [18].

2.3.2.4 3E Set of Three-Dimensional Extended States

The eigenvalues of H_0 are,

$$E_{0,k_{ex},k_{ey},k_{ez}} = \left(V + \hbar^2 k_{ex}^2/2m^*\right) + \left(V + \hbar^2 k_{ex}^2/2m^*\right) + \left(V + \hbar^2 k_{ez}^2/2m^*\right) - V$$
$$= 2V + \hbar^2 k_{ex}^2/2m^* + \hbar^2 k_{ey}^2/2m^* + \hbar^2 k_{ez}^2/2m^* \quad (2.63)$$

The subtracted V sets the energy origin at the barrier material CB bottom. In addition, taking into account Eq. (2.52), the perturbation matrix becomes very simple because

$$\left\langle \tilde{n}_x, \tilde{n}_y, \hat{n}_z \left| U' \right| \tilde{n}'_x, \tilde{n}'_y, \hat{n}'_z \right\rangle = -2V \delta_{\tilde{n}_x, \tilde{n}'_x} \delta_{\tilde{n}_y, \tilde{n}'_y} \delta_{\tilde{n}_z, \tilde{n}'_z} \tag{2.64}$$

In consequence,

$$\left\langle \tilde{n}_x, \tilde{n}_y, \hat{n}_z \left| H \right| \tilde{n}'_x, \tilde{n}'_y, \hat{n}'_z \right\rangle = \left(\hbar^2 k_{ex}^2 / 2m^* + \hbar^2 k_{ey}^2 / 2m^* + \hbar^2 k_{ez}^2 / 2m^* \right) \delta_{\tilde{n}_x, \tilde{n}'_x} \delta_{\tilde{n}_y, \tilde{n}'_y} \delta_{\tilde{n}_z, \tilde{n}'_z} \tag{2.65}$$

which is the same as if the QD were absent although the wavevectors are not plane waves but the product of three 1D extended (in/out phase harmonic) wave corresponding to the k_{ex}, k_{ey} and k_{ez} vectors. Again, in this case, there is a substantial reduction of the H_0 eigenvalues: $2U$ for all of them; however, they do not penetrate into the bandgap, but reach its upper edge. In Fig. 2.6 they are represented by the dark gray zone.

In the box-shaped QD, the continuous spectrum is heavily degenerated (as is visible in Fig. 2.6) and a richer wavefunction structure is possible. For instance, a virtual bound state (0E) may be combined with 1E, 2E and 3E states with the same energy, giving a rather complex eigenfunction that is (as any eigenfunction) a stationary state.

2.4 Absorption Coefficients in Box Shaped Quantum Dots

The radiation (photon) absorption and emission mechanisms in the interaction between the light and a material system, whose foundations were attributed to Dirac by Fermi [21] in 1932, have been extensively presented in textbooks [3, 22, 23]. We have revisited this background for applications associated to solar cells [4]. In this section we follow Ref. [17] closely.

In device physics, the carrier generation rate per unit volume and time is given by the expression [24]

$$g = \int \alpha dF_{ph} = \int \frac{dF_{ph}}{dE} \alpha dE \tag{2.66}$$

where dF_{ph} is an elementary flux of photons per unit area and time in a narrow range of energies and α is the absorption coefficient.

For a single QD, the probability of photon absorption per unit time is given by the Fermi Golden Rule, that in the electric dipole approximation [3] (vol. II, p. 899) is (SI units)

$$w_{|\Xi;N\boldsymbol{q}\rangle \to |\Xi';(N-1)\boldsymbol{q}\rangle} = \frac{N_{ph,\boldsymbol{q}}}{\Omega} \frac{2\pi^2 e^2 E}{n_{ref}^2 h \varepsilon_0} |\langle \Xi | \boldsymbol{r} \cdot \boldsymbol{\epsilon} | \Xi' \rangle|^2 \delta(E_{\Xi'} - E_{\Xi} - E) \qquad (2.67)$$

where $\boldsymbol{\epsilon}$ is the light polarization vector, n_{ref} is the refraction index of the medium, $N_{ph,\boldsymbol{q}}$ is the number of photons in the mode $\boldsymbol{q}$ of energy E and Ω is the crystal volume. This expression represents the number of excitons[5] generated per unit time due to absorption of photons in mode $\boldsymbol{q}$ (which, for the moment, includes the polarization state). It is required that there is an electron in state Ξ, and that state Ξ' is not filled with another electron which would exclude the transition. Furthermore, the spin in the initial and the final state has to be the same. As stated in Eq. (2.28), the matrix element $\langle \Xi | \boldsymbol{r} \cdot \boldsymbol{\epsilon} | \Xi' \rangle$ calculated from the exact wavefunction is the same as that calculated from the envelope function $\langle \Phi | \boldsymbol{r} \cdot \boldsymbol{\varepsilon} | \Phi' \rangle$.

If, in Eq. (2.67), we set

$$\sum_{\boldsymbol{q}} N_{ph,\boldsymbol{q}} / \Omega = n_{ph} \qquad (2.68)$$

we are taking into account exciton generation by all modes with the same energy. The density of photons n_{ph} can be related to the photon flux by $F_{ph} = (c/n_{ref})n_{ph}$. Furthermore, if the fractional coverage of the surface with QDs is F_s and there are N_l QD layers per unit length, the density of QDs per unit volume is $F_s N_l / 4ab$ where $4ab = 4a^2$ is the QD cross-section. With this nomenclature, the exciton generation rate per unit volume and time is

$$g = \int \frac{dF_{ph}}{dE} \frac{2\pi^2 e^2 E}{n_{ref} c h \varepsilon_0} \frac{|\langle \Xi | \boldsymbol{r} \cdot \boldsymbol{\epsilon} | \Xi' \rangle|^2}{4ab} F_s N_l \delta(E_{line} - E) dE \qquad (2.69)$$

where $E_{line} = E_{\Xi'} - E_{\Xi}$. By analogy,

$$\alpha_{\Xi \to \Xi'}^{max} = 2 \frac{2\pi^2 e^2 E}{n_{ref} c h \varepsilon_0} \frac{|\langle \Xi | \boldsymbol{r} \cdot \boldsymbol{\epsilon} | \Xi' \rangle|^2}{4ab} F_s N_l \delta(E_{line} - E) \equiv \alpha_{\Xi \to \Xi'}' E \delta(E_{line} - E) \quad (2.70)$$

where α' is defined for convenience. The first factor of 2 is to account for the spin degeneracy of each state. Furthermore, the superindex *max* in the preceding formulas assumes that there is an electron in the initial state Ξ and none in the final state Ξ'. In general

$$\alpha_{\Xi \to \Xi'} = \alpha_{\Xi \to \Xi'}^{max} f_{\Xi} (1 - f_{\Xi'}) \qquad (2.71)$$

---

[5] Exciton is an electron-hole pair linked by Coulombian attraction. At room temperature excitons are dissociated in a semiconductor. Electron-hole pairs and excitons are often considered synonymous, and is the case in this chapter.

where f_Ξ and $f_{\Xi'}$ are the filling factor (bounded to $0 < f < 1$) of the initial and final electron states. The filling factors are often described as Fermi factors of the type

$$f = \{\exp[(E - E_F)/kT] + 1\}^{-1} \tag{2.72}$$

where E is the energy of the state and E_F is the quasi Fermi level (QFL) for the state in consideration. The QFLs are usually different for the initial and final states except if the sample is in thermal equilibrium, in which case all converge to a single Fermi level.

In most cases, only the fundamental state $|1,1,1\rangle$ is filled with electrons to a significant extent. These electrons often come from donors introduced by doping. All the other states, including those in the CB, are essentially empty. However, this aspect will be further studied when dealing with the detailed balance conditions of the solar cells (Chap. 4). If the doping very strong, or under some other conditions, the first excited state may also become partly filled.

2.4.1 Influence of the Photon Polarization

The matrix element $\langle\Xi|\boldsymbol{\varepsilon}\cdot\boldsymbol{r}|\Xi'\rangle = \cos\phi\sin\theta\langle\Xi|x|\Xi\rangle + \sin\phi\sin\theta\langle\Xi|y|\Xi\rangle + \cos\theta\langle\Xi|z|\Xi'\rangle$ depends on the photon polarization, which is defined here by its Euler angles (φ, θ) with respect to the (x, y, z) axes. In the separation of variables approximation, the matrix element $\langle\Xi|x|\Xi'\rangle = \langle\Phi|x|\Phi'\rangle$ (see Eq. (2.28)) is the product three functions: one depending on x, one depending on y and one depending on z. To have $\langle\Phi|x|\Phi'\rangle \neq 0$ the quantum numbers n_y and n_z must be the same for Φ and Φ' because, otherwise, the internal product of the corresponding one-dimensional wavefunctions is zero, therefore only n_x can vary. What's more, as said before, the quantum numbers must be of different parity: otherwise $\langle\xi|x|\xi'\rangle = 0$. The same can be said for the other coordinates: the only non-zero matrix elements are those for which one single quantum number changes between two states of different parity.

For the SOTA QDs (Table 2.1), whose one-dimensional energies appear in Table 2.2, the matrix elements for polarized light in the direction of the changing QN ($\boldsymbol{\varepsilon}\cdot\boldsymbol{r} = x$ or y or z) can be calculated analytically [17]. They are given in Table 2.6.

Table 2.6 Bound to bound state transitions in the SOTA material for polarized light in the direction of the changing QN

Transition	n_x, n_y				n_z
	$1 \to 2$	$2 \to 3$	$3 \to 4$	$1 \to 4$	$1 \to 2$
E_{line} (eV)	0.100503	0.158622	0.175218	0.434343	0.311947
$|\langle\Phi|\boldsymbol{\epsilon}\cdot\boldsymbol{r}|\Phi'\rangle|^2/4ab$	0.04889	0.03344	0.02868	1.9451×10^{-4}	0.01281

$U = 0.473$ eV; $m^* = 0.0294\ m_0$; $a = b = 8$ nm; $c = 3$ nm; $n_{ref} = 3.5$

As said before, only transitions of different parity in the polarization coordinate are permitted. Among these, the strongest transitions are between consecutive states.

With a general polarization, the square of the module of the matrix element, entering in the absorption coefficient, can be written as:

$$
\begin{aligned}
|\langle \Xi|\boldsymbol{\epsilon}\cdot\boldsymbol{r}|\Xi'\rangle|^2 = {} & \cos^2\varphi\sin^2\theta|\langle\Phi|x|\Phi'\rangle|^2 + \sin^2\varphi\sin\theta^2|\langle\Phi|y|\Phi'\rangle|^2 \\
& + \cos\theta^2|\langle\Phi|z|\Phi'\rangle|^2 + 2\cos\varphi\sin\phi\sin^2\theta\mathrm{Re}[\langle\Phi|x|\Phi'\rangle\langle\Phi|y|\Phi'\rangle] \\
& + 2\cos\varphi\sin\theta\cos\theta\mathrm{Re}[\langle\Phi|x|\Phi'\rangle\langle\Phi|z|\Phi'\rangle] \\
& + 2\sin\varphi\sin\theta\cos\theta\mathrm{Re}[\langle\Phi|y|\Phi'\rangle\langle\Phi|z|\Phi'\rangle]
\end{aligned} \tag{2.73}
$$

Since only one quantum number may vary, the terms containing two different matrix elements are always zero. For instance, if the changing quantum number is n_x, then $\langle\Phi|y|\Phi'\rangle$ is zero and so is the product $\langle\Phi|x|\Phi'\rangle\langle\Phi|y|\Phi'\rangle$. In consequence

$$
|\langle\Xi|\boldsymbol{\epsilon}\cdot\boldsymbol{r}|\Xi'\rangle|^2 = \cos^2\varphi\sin^2\theta|\langle\Phi|x|\Phi'\rangle|^2 + \sin^2\varphi\sin\theta^2|\langle\Phi|y|\Phi'\rangle|^2 + \cos\theta^2|\langle\Phi|z|\Phi'\rangle|^2 \tag{2.74}
$$

and only one of these three terms can be non-zero.

The incident photons have a multitude of polarizations and the observed data results from averaging $|\langle\Xi|\boldsymbol{r}\cdot\boldsymbol{\epsilon}|\Xi'\rangle|^2$. In the case of normal illumination, since the electric field of the photons is transversal, the polarization vector has $\theta = \pi/2$ and $|\langle\Xi|\boldsymbol{r}\cdot\boldsymbol{\epsilon}|\Xi'\rangle|^2 = \cos^2\varphi|\langle\Phi|x|\Phi'\rangle|^2 + \sin^2\varphi|\langle\Phi|y|\Phi'\rangle|^2$. Averaging over all the possible φ form 0 to 2π, we obtain

$$
\left\langle |\langle\Xi|\boldsymbol{\epsilon}\cdot\boldsymbol{r}|\Xi'\rangle|^2 \right\rangle_z = \left(|\langle\Phi|x|\Phi'\rangle|^2 + |\langle\Phi|y|\Phi'\rangle|^2 \right)\big/2 \tag{2.75}
$$

For in-plane illumination, the angle φ is fixed (normal to the propagation of incident light in the plane x, y) and averaging Eq. (2.74) over θ in the interval $(0,\pi)$ we obtain $\cos^2\varphi|\langle\Phi|x|\Phi'\rangle|^2\big/2 + \sin^2\varphi|\langle\Phi|y|\Phi'\rangle|^2\big/2 + |\langle\Phi|z|\Phi'\rangle|^2\big/2$ with only one term being non zero. For instance, if the quantum number that changes is n_y, then the squared matrix element is $\sin^2\varphi|\langle\Phi|y|\Phi'\rangle|^2\big/2$ with lobes in the $\varphi = \pm\pi/2$ that correspond to light beams directed along the x axis. In the case of in-plane illumination it may be that the polarization is fixed, usually either $\theta = 0$ or $\theta = \pi/2$, and that the beam direction is also fixed. In this case Eq. (2.74) must be used without any averaging. In the case of isotropic illumination, as is the case for internal thermal photons emitted spontaneously by the semiconductor, the average is

$$
\left\langle |\langle\Xi|\boldsymbol{\epsilon}\cdot\boldsymbol{r}|\Xi'\rangle|^2 \right\rangle_{isotropic} = |\langle\varphi|x|\varphi'\rangle|^2\big/3 + |\langle\varphi|y|\varphi'\rangle|^2\big/3 + |\langle\varphi|z|\varphi'\rangle|^2\big/3 \tag{2.76}
$$

And, again, only one term is not zero.

Table 2.7 Polarization factor of some bound-to-bound state transitions for several polarization modalities (see nomenclature in text)

Initial	Final	z	x	x/y	x/z
111	121	1/2	1/2	1	0
	211	1/2	0	0	0
	141	1/2	1/2	1	0
	411	1/2	0	0	0
	112	0	1/2	0	1
121	131	1/2	1/2	1	0
	221	1/2	0	0	0
	421	1/2	0	0	0
	122	0	1/2	0	1
211	311	1/2	0	0	0
	221	1/2	1/2	1	0
	241	1/2	1/2	1	0
	212	0	1/2	0	1

Table 2.7 shows the factor that multiplies the element of matrix for all possible transitions between bound states under the assumption that only the fundamental level (1,1,1) and the first excited level with states (1,2,1) and (2,1,1) are appreciably filled with electrons. We consider four examples of illumination: an unpolarized beam in the z direction (denoted z), an unpolarized beam in the x direction (x), a y-polarized beam in the x direction (x/y) and a z-polarized beam in the x direction (x/z). The element of matrix that must be multiplied by this factor is the one whose final state QN differs from that of the initial state. For instance for the transition $|1,2,1\rangle \rightarrow |4,2,1\rangle$ the differing QN are $1 \rightarrow 4$ and the value of the element of matrix is 1.9451×10^{-4}, as found in Table 2.6. This number is to be multiplied by the factor in Table 2.7 corresponding to the beam direction and the polarization of the beam.

2.4.2 Calculation of the Absorption Coefficients Between Bound States in the Separation-of-Variables Approximation

The calculations to follow are based on the separation-of-variables approximation. The use of exact eigenfunctions will be discussed afterwards, and will support the use of this approximation.

We shall consider the cases in which the fundamental state and the first excited state are partially filled with electrons. All the other states are practically empty. Transitions to bound states are Dirac-delta shaped, following Eqs. (2.70) and (2.71). The absorption coefficient for transitions from the fundamental or first excited state to all other bound states is

$$
\begin{aligned}
\alpha^{BS} = {} & f_{1,1,1} \sum_{(n_x,n_y,n_z)\neq(1,1,1)} (1 - f_{n_x,n_y,n_z}) E_{line}\, \alpha'^{n_x,n_y,n_z}_{1,1,1}\, \delta(E_{line} - E) \\
& + f_{1,2,1} \sum_{(n_x,n_y,n_z)\neq(1,1,1),(1,2,1),(2,1,1)} (1 - f_{n_x,n_y,n_z}) E_{line}\, \alpha'^{n_x,n_y,n_z}_{1,2,1}\, \delta(E_{line} - E) \\
& + f_{2,1,1} \sum_{(n_x,n_y,n_z)\neq(1,1,1),(1,2,1),(2,1,1)} (1 - f_{nx,ny,nz}) E_{line}\, \alpha'^{n_x,n_y,n_z}_{2,1,1}\, \delta(E_{line} - E)
\end{aligned}
$$

$$(2.77)$$

where E_{line} is in each instance the energy difference between the final and initial state. The number of totally bound states in the QD is finite and usually restricted to few states. Note that $f_{1,2,1} = f_{2,1,1}$. In the α's, the subindices and superindices are the QNs of the initial and final states respectively.

The Dirac delta is in practice a narrow line whose width is controlled by the QDs' homogeneity. Small variations of size lead to line broadening. Broadening may also come from variations in the band offset or the effective mass. In practice, we use a Gaussian distribution such that

$$
\delta(E - E_{line}) \cong \frac{1}{\sigma\sqrt{\pi}} \exp\left(-\frac{(E - E_{line})^2}{\sigma^2} \right) \tag{2.78}
$$

In our calculations, we have set the energy dispersion $\sigma = 0.025$ eV.

Optimal filling for IB solar cells requires the fundamental state to be partially filled and the first excited state to be empty. For Quantum Dot Infrared Photodetectors (QDIPs) the fundamental state should be totally filled and the first excited state should be empty. Focusing our study on intermediate band solar cells, we present in Fig. 2.8 the absorption coefficients for the case (a) $f_{1,1,1} = 0.5$, $f_{1,2,1} = f_{2,1,1} = 0$ and for the case (b) $f_{1,1,1} = 1$, $f_{1,2,1} = f_{2,1,1} = 0.5$ corresponding to overdoping. The second might be the sought doping for QDIPs. The illumination conditions are specified in the figure caption.

Compared to the first case, the second case leads to a much stronger absorption and exhibits a peak at 0.159 eV that is absent in the first case. What is more, there is a reduction in the intensity of the first peak relative to the last peak. The different beam directions and polarizations have a strong influence on the absorption spectrum. In particular, the in-plane unpolarized illumination reduces the absorption by half at the 0.101 eV line with respect to the normal unpolarized illumination, but produces an additional absorption at the 0.312 eV line. It is to be stressed that there is strong influence of the filling state on the absorption coefficients. We might expect the peak at almost 0.1 eV to partially fill level (1,2,1) due to transitions from the level (1,1,1), and therefore the exclusive filling of the first level may not be realistic. The same can be said with the transitions of level (1,2,1) to level (2,2,1). A detailed balance analysis, to be presented later, will give us knowledge on the filling states and therefore a better vision of the absorption coefficients.
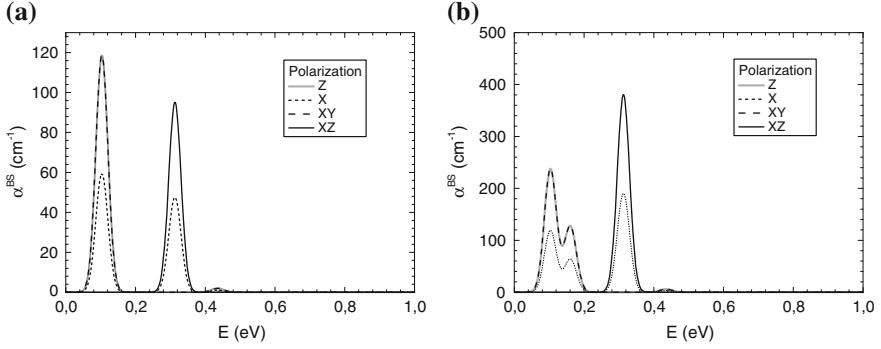
Fig. 2.8 Absorption coefficient due to transitions between bound states. *Grey solid line* z (normal) unpolarized beam; *black dotted line* x unpolarized beam; *black dashed line* y-polarized x-beam; *black solid line* z-polarized x-beam. **a** The fundamental (1,1,1) state is filled to 50 %. **b** The fundamental state is filled to 100 % and the first excited states (1,2,1) and (2,1,1) are filled to 50 %. $\sigma = 0.025$ eV. The 0.101 eV peak corresponds to (1,1,1) $\rightarrow$ (1,2,1), the 0.159 eV peak to (1,2,1) $\rightarrow$ (2,2,1), the 0.312 eV peak to (1,1,1) $\rightarrow$ (1,1,2) and the 0.434 eV peak to (1,1,1) $\rightarrow$ (1,4,2). QD data as in the SOTA prototype. Reproduced with permission. © 2013, Elsevier [25]

2.4.3 The Absorption Coefficients with Exact Eigenfunctions

One of the benefits of the separation of variables is the easy labeling of the states. The eigenfunctions in the exact solutions of Sect. 2.3.2 are clearly defined as linear combination of separable states but a concise labeling for them is difficult if it has to be illustrative.

Here, we label the states with their energies followed by (1) or (2) added to distinguish the first and second state listed in Table 2.5, when the states are degenerate. Using this table, that spans the exact states in the basis of separable states, and taking into account the forbidden transitions,

$$\begin{aligned}
\langle -0.271|x|-0.174(1)\rangle &= -0.083\langle 1,1,1|x|2,1,1\rangle \\
\langle -0.271|y|-0.174(1)\rangle &= 0.996\langle 1,1,1|y|1,2,1\rangle
\end{aligned} \tag{2.79}$$

For vertical unpolarized illumination the two preceding terms must be squared, added and divided by 2, as discussed in Sect. 2.4.1. According to Table 2.6, the values $\langle 1,1,1|x|2,1,1\rangle/4ab = \langle 1,1,1|y|1,2,1\rangle/4ab = 0.04889$ whereas $\langle 1,1,1|x|1,2,1\rangle/4ab = 0$ and $\langle 1,1,1|y|1,2,1\rangle/4ab = 0.04889$. Therefore

$$\left(\frac{|\langle -0.271|x|-0.174(1)\rangle|^2}{4ab} + \frac{|\langle -0.271|y|-0.174(1)\rangle|^2}{4ab}\right)\Bigg/2 = 0.02442$$

$$\left(\frac{|\langle 1,1,1|x|1,2,1\rangle|^2}{4ab} + \frac{|\langle 1,1,1|y|1,2,1\rangle|^2}{4ab}\right)\Bigg/2 = 0.02445 \tag{2.80}$$

which shows a negligible influence of the use of the exact states. Nevertheless some transitions that are forbidden in the separation of variables approximation may appear permitted with the exact states, but associated to negligible values of the absorption coefficients.

2.4.4 Calculation of the Absorption Coefficients Between Bound and Extended States

The transitions between bound states and extended states must fulfill also the rules of selection: initial and final states differ only in one QN and the (one-dimensional) parity of the initial and final states must be different. In consequence the final states have to belong to the type 1E, that is, they are extended only in one dimension.

We consider transitions from the fundamental or the first excited state, which are assumed to be the only states filled with electrons. We use the variable ρ to denote the extended dimension ($\rho = x$ or y or z). Only transitions to the extended states with parity different to the (one-dimensional) bound states are permitted. The separation between two such transitions of the same parity for large L, taking into account Eq. (2.43), which gives the values of the wavevector for a given QN, is,

$$\Delta k_{odd} = \Delta k_{even} = \pi/L. \tag{2.81}$$

Therefore, looking at the relationship between wavevectors and energies in Eq. (2.41), the density $N(E_{k_e;\rho})$ of extended states per unit of energy.

$$N(E_{k_e;\rho}) = \frac{1}{\Delta k_{even}} \frac{dk_e}{dE_{k_e;\rho}} = \frac{1}{\Delta k_{odd}} \frac{dk_e}{dE_{k_e;\rho}} = \frac{L(m^*)^{1/2}}{2^{1/2}\hbar\pi} E_{k_e;\rho}^{-1/2} \tag{2.82}$$

For the case $\rho = x$, the energy of the absorbed photons E_{line} is now

$$E_{line} = E_{0,k_e,n_y,n_z} - E_{0,n_x,n_y,n_z} = E_{k_e;x} - E_{n;x} \tag{2.83}$$

where $E_{k_e;x}$ and $E_{n;x}$ represent the one-dimensional energies in the x-direction. The same can be said for the other variables.

For the transition from a bound state to a state extended in one dimension we use the notation $\alpha'_{n;\rho}(k_e)$ where n is the initial value of the changing quantum number with corresponding coordinate ρ, and k_e corresponds to the final state wavevector outside the QD well, corresponding to the same coordinate.

The absorption coefficient for transitions from a bound state to all the 1E states is then

$$\alpha_{n;\rho}^{ES}(k_e) = f_{n_x,n_y,n_z} \sum_k (1 - f_C)E\alpha'_{n;\rho}(k_e)\delta(E_{line} - E)$$

$$\cong f_{n_x,n_y,n_z} \int N(E_\rho)E\alpha'_{n;\rho}(k_e)\delta(E_{line} - E)dE \qquad (2.84)$$

$$= f_{n_x,n_y,n_z}N(E_{line} + E_{n;\rho})E_{line}\alpha'_{n;\rho}\big(k_e(E_{line} + E_{n;\rho})\big)$$

Taking into account that only the fundamental and first excited states have appreciable probability of occupation, we can write

$$\alpha^{ES} = \sum_{\rho=x,y} \sum_{n=1,2} f_{n,1,1} \sum_{k_u} N(E_{line} + E_{n;\rho})E_{line}\alpha'_{n;\rho}\big(k_u(E_{line} + E_{n;\rho})\big) \qquad (2.85)$$

where the sums must take into account all the combinations of possible transitions between bound states and the possible final extended state for each bound state.

There is a polarization influence in the calculation of the $\alpha'_{n;\rho}(k_e)$. It is presented in Table 2.8. The absorption coefficient is given by Eq. (2.85) summing over all the transitions found in this table. The matrix elements, which are analytic, are given in Ref. [17] (appendices). The $\alpha'_{u;n}$ are calculated with the absorption coefficient formula of Eq. (2.70).

The functions $\alpha_{n,\rho}^{ES}(k_e)$ defined in Eq. (2.85) are zero for photon energies below $E_{n;\rho}$. To account for this, we could multiply them by a step function starting at $E_{n;\rho}$. However, in the same way we have used a Gaussian function, instead of a Dirac delta, to account for the dispersion of the QDs size, here we can replace the step function with

$$H(E - E_{line}) \cong \left[\exp\left(-\frac{E - E_{u;n}}{2\sigma}\right) + 1\right]^{-1} \qquad (2.86)$$

Table 2.8 Polarization factor of some bound-to-extended state transitions for several polarization modalities (see nomenclature in text)

Initial	Final	z	x	x/y	x/z
111	$1k1$	1/2	1/2	1	0
	$k11$	1/2	0	0	0
	$11k$	0	1/2	0	1
121	$1k1$	1/2	1/2	1	0
	$k21$	1/2	0	0	0
	$12k$	0	1/2	0	1
211	$2k1$	1/2	1/2	1	0
	$k11$	1/2	0	0	0
	$21k$	0	1/2	0	1

(a)

(b)
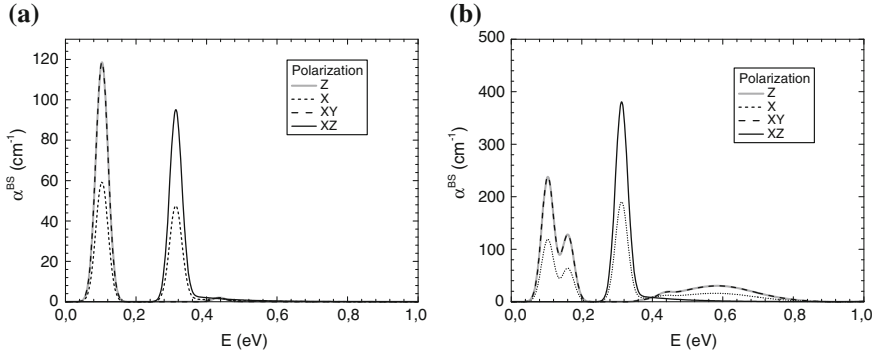
Fig. 2.9 Absorption coefficient due to transitions between bound to bound and bound to extended states. *Grey solid line* z (normal) unpolarized beam; *black dotted line* x unpolarized beam; *black dashed line* y-polarized x-beam; *black solid line* z-polarized x-beam. **a** The fundamental (1,1,1) state is filled to 50 %. **b** The fundamental state is filled to 100 % and the first excited states (1,2,1) and (2,1,1) are filled to 50 %. $\sigma = 0.025$ eV (This plot includes a correction of the results in [25] (which inspires this subsection) consisting on a wrong sign in a formula and an inaccurate normalization of the extended functions. We thank Aleksandr Panchak for calculations)

With $\sigma = 0.025$ eV. In Fig. 2.9 we present the absorption coefficients $\alpha^{BS} + \alpha^{ES}$ for the cases (a) $f_{1,1,1} = 0.5$, $f_{1,2,1} = f_{2,1,1} = 0$ and (b) $f_{1,1,1} = 1$, $f_{1,2,1} = f_{2,1,1} = 0.5$.

By comparing these plots with those in Fig. 2.8, we realize that the main part of the transitions is between bound states. Transitions to the extended states form tails of less importance. We insist here that the filling of states considered in this subsection may be unrealistic and a detailed balance analysis will be necessary for a realistic evaluation of the absorption. As a matter of fact, the absorptions studied in this subsection will fill the upper states leading to transference of the electrons from them to states of higher energy and ultimately to the CB. On the other hand, it is well known (and we shall see it later in this book) that absorption and emission of photons are strongly linked. This means that concurrent with the upwards traffic of electrons produced by the absorption of light there is a downwards traffic due to the emission of photons, stronger if the absorption coefficient is stronger and weaker if it weaker.

Additionally, we may observe that much of the absorption is produced at energies that are small. At room temperature the semiconductor contains an abundance of thermal photons at these energies. Often many more than those that can be injected by the sun inside the semiconductor. Table 2.9 shows the ratio of

Table 2.9 The ratio of externally incident to internal ambient photon density is also calculated for the line energies for AM0 illumination of 0.136 W $\cdot$ cm^{-2} (0.0121 W $\cdot$ cm^{-2} below 0.726 eV)

|	$n_x, n_y,$ $1 \rightarrow 2$	$n_x, n_y,$ $2 \rightarrow 3$	$n_x, n_y,$ $3 \rightarrow 4$	$n_x, n_y,$ $1 \rightarrow 4$	$n_z,$ $1 \rightarrow 2$
Energy (eV)	0.100503	0.158622	0.175218	0.434343	0.311947
External/internal ph. (1AM0 suns)	0.00009452	0.00054350	0.00091954	6.28179	0.088276

photons from an external AM0 source at the extraterrestrial radiation level $(0.136 \text{ W cm}^{-2})$ and internal thermal photons at 300 K. For most levels, this ratio is, in the absence of concentration, well below one.

The consequence of this is that electrons may be pumped up, towards the CB, by these thermal photons. It might seem that this is very good; however, in reality, energy cannot be extracted from them unless the second law of thermodynamics is violated. The topic is discussed in [26]. In fact, we shall see that this strong up- and downwards communication between the IB levels and the CB via thermal photons prevents the splitting of their QFLs. This renders the IB levels a mere extension of the CB into the forbidden band and ultimately leads to a reduction in the open circuit voltage. The IB levels can be thus considered as ladder states for this communication between the IB states and the CB. The use of a host material of higher bandgap than the GaAs, such as the GaAlAs, may reduce the thermal escape and the drawbacks associated to it.

2.5   Experimental Measurement of the Intermediate Band to Conduction Band Absorption

The absorption studied in this chapter has been measured on several occasions [27–29]. In general, a waveguide like the one depicted in Fig. 2.10a is used to increase the optical path inside the QD material. An example of the measured absorption is presented in Fig. 2.10b.

Fig. 2.10 Light absorption of low energy photons corresponding to the intraband transitions studied in this chapter. **a** 45° waveguide. **b** Absorbance for InAs QDs in GaAs and GaAlAs barrier materials. Reproduced with permission. © 1997 AIP [27]
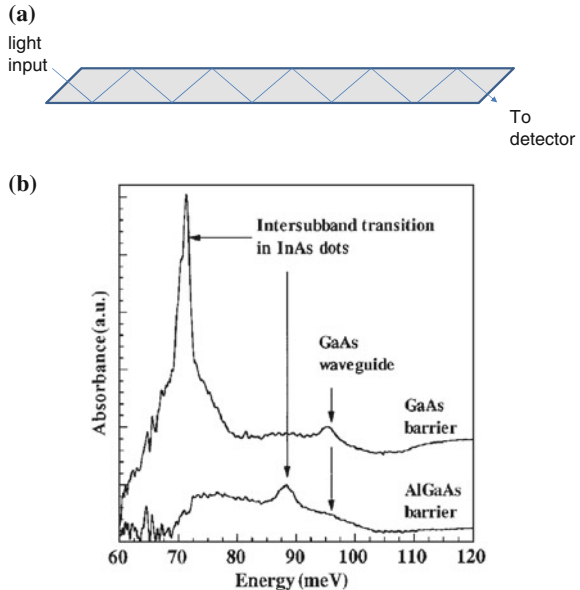
Strong absorption is found at about 0.07 eV for the InAs/GaAs structure; this represents a photon energy below the one calculated in Fig. 2.9. This is not surprising since the position of the levels depends strongly on the QD size. Other experiments show the main peak at around 0.15 eV [28]. Also, the barrier material, which affects to the offset potential, affects the position of the absorption lines.

2.6 Spherical Quantum Dots

2.6.1 Central Potential Hamiltonian

In this section we are going to calculate the energy spectrum and the eigenfunctions of a QD with spherical shape and square potential.

In spherical coordinates, the envolvent TISE is [3]

$$
\begin{aligned}
&\left(\frac{p_r^2}{2m^*} + \frac{\hat{l}^2}{2m^*r^2} + U(r)\right)\Phi(r,\theta,\varphi) = E\Phi(r,\theta,\varphi) \\
&p_r \equiv \frac{\hbar}{i}\frac{1}{r}\frac{\partial}{\partial r}r \\
&\hat{l}^2 \equiv -\frac{\hbar^2}{\sin^2\theta}\left[\sin\theta\frac{\partial}{\partial\theta}\left(\sin\theta\frac{\partial}{\partial\theta}\right) + \frac{\partial^2}{\partial\varphi^2}\right]
\end{aligned} \tag{2.87}
$$

$\hat{l}$ has a physical meaning; it is the kinetic moment $\boldsymbol{r} \times \boldsymbol{p}$.

It is visible that $\hat{l}^2$ (only depending on angular variables) commutes with the Hamiltonian. Therefore, there is a basis of eigenfunctions that are simultaneously eigenfunctions of the Hamiltonian and of $\hat{l}^2$. Let us look first for the $\hat{l}^2$ eigenfunctions.

$$
\hat{l}^2 Y_l^m(\theta,\varphi) = l(l+1)Y_l^m(\theta,\varphi) \tag{2.88}
$$

where $Y_l^m(\theta,\varphi)$ are the well-known spherical harmonics; l can take the values 0, 1, 2, 3,... and m can take the values $-l, -l+1,... 0,... l-1, l$. The equation is verified if $Y_l^m(\theta,\varphi)$ is multiplied by any constant or even by a function not depending on (θ,φ). In particular, we can use an arbitrary function of r such as $f(r)$. By introducing $f(r)Y_l^m(\theta,\varphi)$ into Eq. (2.87) we obtain the so called radial equation,

$$
-\frac{\hbar^2}{2m^*}\left(\frac{\partial^2 f(r)}{\partial r^2} + \frac{2}{r}\frac{\partial f(r)}{\partial r}\right) + \left(\frac{l(l+1)}{2m^*r^2} + U(r) - E\right)f(r) = 0 \tag{2.89}
$$

Table 2.10 Some expanded spherical Bessel functions

| l	$j_l(kr)$	$-n_l(kr)$	$-i^l h_l^{(+)}(i\kappa r)$
0	$\dfrac{\sin(kr)}{kr}$	$-\dfrac{\cos(kr)}{kr}$	$-\dfrac{\exp(-\kappa r)}{kr}$
1	$-\dfrac{\cos(kr)}{kr}+\dfrac{\sin(kr)}{(kr)^2}$	$-\dfrac{\cos(kr)}{kr}-\dfrac{\sin(kr)}{(kr)^2}$	$\dfrac{i\exp(-\kappa r)(1+\kappa r)}{(\kappa r)^2}$
2	$-\dfrac{3\cos(kr)}{(kr)^2}+\dfrac{\left(3-(kr)^2\right)\sin(kr)}{(kr)^3}$	$-\dfrac{3\sin(kr)}{(kr)^2}-\dfrac{\left((3-(kr)^2\right)\cos(kr)}{(kr)^3}$	$\dfrac{\exp(-\kappa r)\left(3+3\kappa r+(\kappa r)^2\right)}{(\kappa r)^4}$
3	$\dfrac{\left(-15+(kr)^2\right)\cos(kr)}{(kr)^3}$ $-\dfrac{\left(-15+6(kr)^2\right)\sin(kr)}{(kr)^4}$	$\dfrac{\left(-15+(kr)^2\right)\sin(kr)}{(kr)^3}$ $+\dfrac{\left(-15+6(kr)^2\right)\cos(kr)}{(kr)^4}$	$-i\exp(-\kappa r)$ $\times\dfrac{\left(15+15\kappa r+6(\kappa r)^2+(\kappa r)^3\right)}{(\kappa r)^4}$

In the case of a constant potential $U(r) = V_0$

$$\left(\frac{\partial^2 f(kr)}{\partial(kr)^2}+\frac{2}{r}\frac{\partial f(kr)}{\partial(kr)}\right)+\left(1-\frac{l(l+1)}{(kr)^2}\right)f(kr)=0$$

$$\text{with}\quad k=\frac{\sqrt{2m^*(E-V_0)}}{\hbar}$$

(2.90)

This is the spherical Bessel equation. Its general solution is a linear combination of two particular solutions, e.g. the functions $j_l(kr)$ and $n_l(kr)$ (see definitions in [3, Appendix B]) whose asymptotic behavior for kr $\rightarrow \infty$ is $\sin(kr - l\pi/2)/kr$ and $\cos(kr - l\pi/2)/kr$ respectively. However, only $j_l(kr)$ is acceptable; at the origin $j_l(kr) \rightarrow (kr)^l$, whereas $n_l(kr)$ diverges at the origin as $n_l(kr) \rightarrow (kr)^{-l-1}$, which is not acceptable. The functions $h^{(+)} \equiv n_l + ij_l$ and $h^{(-)} \equiv n_l - ij_l$, with asymptotic behavior $\exp(i(kr - l\pi/2))/kr$ and $\exp(-i(kr - l\pi/2))/kr$ are also acceptable in some cases.

For a given l index, the spherical Bessel functions may be expanded into more common functions. We present in Table 2.10 these expansions for some values of l. A drawing of some of these functions is presented in Fig. 2.11.
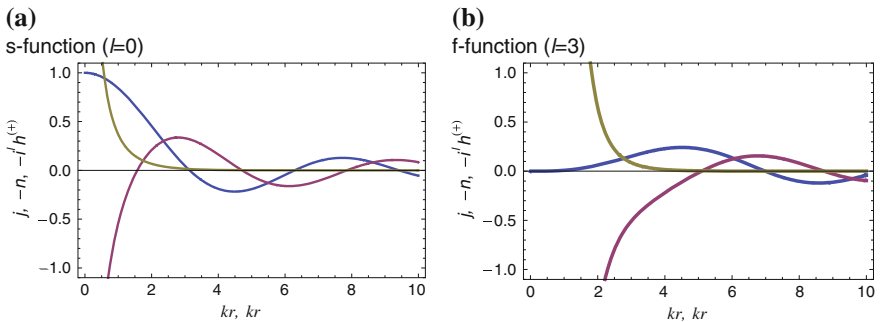
Fig. 2.11 Some spherical Bessel functions. *Blue*, $j_l(kr)$; *red*, $-n_l(kr)$; *yellow*, $-i^l h_l^{(+)}(i\kappa r)$ (color figure online)

2.6.2 Quantum Dots of Spherical Symmetry and Square Potential

If now we consider the case of a square potential, such that $V_0 = -V$ for $r \leq a$ and $V_0 = 0$ for $r > a$ (the origin of energies has been put at the host semiconductor CB) we have two cases:

For $E < 0$, we can define $i\kappa \equiv k$ so that $\kappa = (-2\,m^*E)^{1/2}$. Outside the QD $(r > a)$ only the solutions with an exponentially decreasing behavior can be accepted; if this is the case, the only acceptable solution is $h^{(+)}(kr) = h^{(+)}(i\kappa r)$ (with an arbitrary constant); inside the QD $(r \leq a)$, $k_i \equiv (2\,m^*(E + V))^{1/2}$ and only the solution $j_l(k_ir)$ is acceptable (with an arbitrary constant). Both have to coincide ar $r = a$ as well as their fist derivative. Therefore the condition

$$\frac{dh^+(i\kappa r)}{dr} \Big/ h^+(i\kappa r) = \frac{dj(k_ir)}{dr} \Big/ j(k_ir) \tag{2.91}$$

has to be fulfilled. This leads to a set of discrete values for the energy. Note that the Bastard boundary conditions of Sect. 2.2.2 can also be applied to this case.

For $E > 0$, is $C_1 j_l\,(k_ir)$ inside the QD and $C_2[\cos(\delta_l)j_l\,(k_er) + \sin(\delta_l)C_2 n_l(k_er)]$ with C_1, C_2 and δ_l three arbitrary constants and $k_e \equiv (2\,m^*E)^{1/2}$. The matching of function and derivative lead to

$$k_e \frac{d(\cos(\delta_l)j_l(k_er) + \sin(\delta_l)n_l(k_er))}{dr} \Big/ (\cos(\delta_l)j_l(k_er) + \sin(\delta_l)n_l(k_er))$$
$$= k_i \frac{dj(k_ir)}{dr} \Big/ j(k_ir) \tag{2.92}$$

and this determines δ_l. Note that, in this case, any value of E is valid and the spectrum is continuous.

2.6.3 Spherical Symmetry and the Cubic Case

The current method of QD growth, consisting in growing InAs layers on a GaAs substrate in a molecular beam epitaxy (MBE) apparatus, tends to produce squat QDs. Some studies on QDs assume that they are spherical. This is a good approximation for colloidal QDs. However, the differences between squat cubic and spherical QDs are substantial.

In spherical QDs, no virtual bound states are found for a large variety of potential profiles, provided that they tend to zero (the wellhead energy) fast enough.

Smaller QDs are desirable for many applications and they have often been studied under the spherical symmetry. We analyze now a cubic box-shaped QD of dimensions $6 \times 6 \times 6$ nm^3 (the same height of the present QDs) and leave the

Table 2.11 Eigenvalues E_0 of the separation-of-variables Hamiltonian H_0 presented in increasing order and 1st order approximations E due to the perturbation potential V' for wavefunctions of the class 0E (bound states). The energy origin is located at the barrier material CB bottom. The 1st order approximation is exact

State	$|1,1,1\rangle$	$|2,1,1\rangle$	$|1,2,1\rangle$	$|1,1,2\rangle$	$|2,2,1\rangle$	$|2,1,2\rangle$	$|1,2,2\rangle$	$|2,2,2\rangle$
E_0 (eV)	−0.0681	0.2105	0.2105	0.2105	0.4891	0.4891	0.4891	0.7677
E (eV)	−0.0890	0.1385	0.1385	0.1385	0.2767	0.2767	0.2767	0.3728

remaining parameters unchanged. For the bound states we obtain Table 2.11. In this case, the 1st order approximation, studied in Sect. 2.3, coincides with the exact solution. The exact eigenvectors are the separation-of-variables solutions denoted in the table.

A spherical QD with the same volume as the $6 \times 6 \times 6$ nm^3 cube has a diameter of 7.4 nm and the s-state ($l = 0$) energy is −0.0902 eV, rather close to the only below-bandgap bound state energy of −0.0890 eV obtained for the cube. In the sphere this is the only bound state; neither a second s-state nor states with any other angular symmetry are present for the parameters used. Thus, the absence of virtual bound states is a singularity of the high symmetry of the spherical QD.

In the cube, there are also eigenfunctions that are extended in one dimension or in two dimensions and bound in the remaining ones. Their continuous spectrum starts well inside the host material CB. Values are not reported for lack of specific interest. These types of solutions are also missing in the spherical QDs.

Apparently, the spherical-wave solutions are missing in the cube. Actually this is not true. A spherical wave can be built as continuous linear combination of plane waves. All the $\boldsymbol{k}$-vectors of module k are the components. In effect, let us analyze the function

$$\Phi(\boldsymbol{r}) = \int \delta(|\boldsymbol{k}| - k) \exp(i\boldsymbol{k} \cdot \boldsymbol{r}) d^3k = 2\pi k^2 \int_0^\pi \exp(ikr\cos\vartheta) \sin\vartheta d\vartheta = \frac{4\pi k}{r} \sin(kr)$$

(2.93)

where ϑ is the angle between the vectors $\boldsymbol{k}$ and $\boldsymbol{r}$ (spherical coordinates in the $\boldsymbol{k}$-space are used and the polar-axis is taken to be in the direction of $\boldsymbol{r}$). For the final result, the change of variables $\cos\vartheta = u$ has been made.

For large values of r, the function $\exp(i\boldsymbol{k} \cdot \boldsymbol{r})$ is also an eigenstate of the box-shaped potential well, as is the function $\exp(-i\boldsymbol{k} \cdot \boldsymbol{r})$. To prove this, let us go back to the one dimensional eigenfunctions,

$$e^{ik_x x} = \frac{(e^{i\theta_o}\xi_{k,e} + ie^{i\theta_e}\xi_{k,o})}{\cos(\theta_o - \theta_e)}$$

$$e^{-ik_x x} = \frac{(e^{-i\theta_o}\xi_{k,e} - ie^{-i\theta_e}\xi_{k,o})}{i\sin(\theta_e - \theta_o)}$$

(2.94)

In the first octant (where all the space coordinates are positive) the exponential is developed in the eigenfunctions described above as (e and o mean even and odd respectively)

$$
\begin{aligned}
e^{i\boldsymbol{k}\cdot\boldsymbol{r}} =\ & \frac{e^{i(\theta_{xo}+\theta_{yo}+\theta_{zo})}\big|k_x e, k_y e, k_z e\big\rangle + i e^{i(\theta_{xo}+\theta_{yo}+\theta_{ze})}\big|k_x e, k_y e, k_z o\big\rangle}{\cos(\theta_{xo}-\theta_{xe})\cos(\theta_{yo}-\theta_{ye})\cos(\theta_{zo}-\theta_{ze})} \\[4pt]
& + \frac{i e^{i(\theta_{xo}+\theta_{ye}+\theta_{zo})}\big|k_x e, k_y o, k_z e\big\rangle + i e^{i(\theta_{xe}+\theta_{yo}+\theta_{zo})}\big|k_x o, k_y e, k_z e\big\rangle}{\cos(\theta_{xo}-\theta_{xe})\cos(\theta_{yo}-\theta_{ye})\cos(\theta_{zo}-\theta_{ze})} \\[4pt]
& - \frac{e^{i(\theta_{xo}+\theta_{ye}+\theta_{ze})}\big|k_x e, k_y o, k_z o\big\rangle + e^{i(\theta_{xe}+\theta_{yo}+\theta_{ze})}\big|k_x o, k_y e, k_z o\big\rangle}{\cos(\theta_{xo}-\theta_{xe})\cos(\theta_{yo}-\theta_{ye})\cos(\theta_{zo}-\theta_{ze})} \\[4pt]
& - \frac{e^{i(\theta_{xe}+\theta_{ye}+\theta_{zo})}\big|k_x o, k_y o, k_z e\big\rangle i e^{i(\theta_{xe}+\theta_{ye}+\theta_{ze})}\big|k_x o, k_y o, k_z o\big\rangle}{\cos(\theta_{xo}-\theta_{xe})\cos(\theta_{yo}-\theta_{ye})\cos(\theta_{zo}-\theta_{ze})}
\end{aligned}
\tag{2.95}
$$

In other octants, the linear combination is somewhat different insofar as the de-phasing angles change the sign for the negative coordinate. For the wave plane travelling backwards, a slightly different linear combination is to be built.

Once the plane wave is built, a linear combination of them leads to the spherical wave of Eq. (2.93). Notice that, in the context of this paper, the $\boldsymbol{k}$s are restricted to the first octant in the $\boldsymbol{k}$-space. However, the same result is obtained if the linear combination $\exp(i\boldsymbol{k}\cdot\boldsymbol{r}) + \exp(-i\boldsymbol{k}\cdot\boldsymbol{r})$ is integrated.

As is well known, plane waves can also be obtained as a linear combination of spherical waves (see e.g., [3]). Thus, the main difference between the spherical and box-shaped square-potential-well QDs is that the latter presents virtual 0E bound states and linear and planar 1E and 2E extended states, all absent in the spherical QD. It has to be stressed that the solutions we are presenting here are exact solutions for the model described. The same model is used for the spherical QD with only the change of shape.

2.7 Concluding Remarks of This Chapter

In this chapter, we have described the effective mass Schrödinger equation to calculate the envelope functions used to describe the eigenfunctions and calculate the eigenvalues of nanostructured semiconductors in the cases where a single band envelope equation is a good approximation. This is usually the case of the conduction band eigenfunctions in zincblende semiconductors. The requirement is that the function $u_{v,\boldsymbol{k}}$ is independent of $\boldsymbol{k}$ at least for small values of this parameter.

In our calculations, a box-shaped QD is studied in detail. The CB band offset between QD and host is assumed square (for comparison with more accurate calculations, look at [30, 31]). The QD is assumed to be box shaped. We believe that these two assumptions are a reasonable representation of the real QDs in zincblende semiconductors, and indeed easier to treat. A separation-of-variables solution of the

box shape allows an easy labeling of the eigenstates thorough a set of three QNs corresponding to the one-dimensional eigenfunctions, the eigenvalues being the sum of the one-dimensional eigenvalues. An exact solution of the mathematical problem of the box-shaped square potential, obtained by diagonalization of this Hamiltonian in the basis of separation-of-variables eigenfunctions, confirm the existence of virtual bound states that are sometimes described as resonances of extended wavefunctions and whose existence is even a matter of doubt by some authors [32, 33] based on mathematical grounds. In this chapter, they are very clearly proven, also based on mathematical grounds, and play a very important role in the light absorption processes.

It is also found that the separation-of-variables energy spectrum (the eigenvalues) is accurate for the IB states and for the lower energy virtual bound states, but it is not acceptable for the higher energy virtual bound states. It is exact for extended states. A first-order energy approximation is reasonably accurate for some applications in the case of high energy virtual bound states.

In the nanostructured semiconductors, we use at least two different semiconductors, the barrier or host semiconductor and the nanostructure semiconductor. As implied in the preceding text, much of the potential in the nanostructured material is due to the CB offset between host and nanostructure. But also the effective masses are different in the nanostructure and the host. As a rule, this is not taken into consideration in our studies. We generally use the QD effective mass everywhere. We also recommended using the host material effective mass for the study of extended states (although this recommendation is not followed in the examples presented). There is also the possibility of using a Hermitical effective mass energy operator that applies for variable effective mass. The reason we do not use it is because it is not theoretically compatible with our basic assumption of a position-variable energy-dispersion function, though it must be mentioned that a position-variable energy-dispersion function is per se a doubtful concept. However, leaving aside the doubtfulness of the concept, in the separation of variables approximation, using the boundary conditions at the QD edges implied by the variable-effective-mass energy operator (the Bastard boundary conditions) leads to a bound-state energy spectrum that is close that obtained using the QD effective mass for the low energies and close to that obtained using the host material effective mass for the high energies. In summary, it seems that the eigenvalues and probably the eigenfunctions obtained using a position-variable effective mass are more accurate than using the approach we propose. However, to verify this statement, it is necessary to find the solution of the exact equation in the framework presented in this book, which is more difficult and has not been undertaken so far. The same can be said about the light absorption properties resulting for the use of this approximation.

A very interesting conclusion of this chapter is that the absorption properties, in the one band effective mass approximation, depend only on the envelope functions and these depend on the material only through the offset potential and the effective mass. Otherwise they depended mainly on the shape and size of the QD. This is very good because the knowledge of the periodic part of the Bloch function is a

serious problem. This statement is only true if the integral multiplication rule can be applied and would not be true for too small QDs.

In this context, the workhorse of the absorption of light is produced between bound states in the IB and virtual bound states in the CB. One-dimensional extended states, a modality specific to the box-shaped QDs, play a secondary role in the light absorption. Spherical QDs have neither virtual bound states nor states which are partially bound and partially extended (like the one dimensional extended states). In conclusion, it is probable that they absorb the light more weakly than the extended states, but this cannot be ascertained without a specific calculation.

Experimental confirmation of the calculations of this chapter is also presented, although in structures we have not analyzed theoretically so that any attempt of quantitative confirmation is not possible.

Finally, it seems that the large QDs produced in the Stransky Krastanov growth mode leads to excited states of the IB that, at least in the InAs/GaAs QD/host system, lead to what we call ladder states able to absorb the abundant thermal photons and putting in thermal contact IB and CB. This results in a reduction of the solar cells open circuit voltage. In fact, this reduction totally disappears at low temperatures [9, 34] at which the bandgap voltage is almost fully achieved.

References

1. Datta S (1989) Quantum phenomena. Molecular series on solid state devices, vol 8. Addison Wesley, Reading
2. Kaxiras E (2003) Atomic and electronic structure of solids. Cambridge University Press, New York
3. Messiah A (1960) Mécanique quantique. Dunod, Paris
4. Luque A, Marti A, Mendes MJ, Tobias I (2008) Light absorption in the near field around surface plasmon polaritons. J Appl Phys 104(11):113118. doi:10.1063/1.3014035
5. Luque A, Antolín E, Linares PG, Ramiro I, Mellor A, Tobías I, Martí A (2013) Interband optical absorption in quantum well solar cells. Sol Energy Mater Sol Cells 112:20–26. doi:10.1016/j.solmat.2012.12.045
6. Bastard G (1990) Wave mechanics applied to semiconductor nanostructures. Monographies de Physique. Les Editions de Physique, Paris
7. Antolín E, Marti A, Farmer CD, Linares PG, Hernández E, Sánchez AM, Ben T, Molina SI, Stanley CR, Luque A (2010) Reducing carrier escape in the InAs/GaAs quantum dot intermediate band solar cell. J Appl Phys 108(6):064513
8. Martí A, Antolín E, Cánovas E, López N, Luque A, Stanley C, Farmer C, Díaz P, Christofides C, Burhan M (2006) Progress in quantum-dot intermediate band solar cell research. In: Poortmans J, Ossenbrink H, Dunlop E, Helm P (eds) Proceedings of the 21st European photovoltaic solar energy conference. WIP-Renewable Energies, Munich, pp 99–102
9. Linares PG, Marti A, Antolin E, Farmer CD, Ramiro I, Stanley CR, Luque A (2012) Voltage recovery in intermediate band solar cells. Sol Energy Mater Sol Cells 98:240–244. doi:10.1016/j.solmat.2011.11.015
10. Luque A, Marti A, Antolín E, Linares PG, Tobias I, Ramiro I (2011) Radiative thermal escape in intermediate band solar cells. AIP Adv 1:022125
11. Antolín E, Martí A, Luque A (2011) The lead salt quantum dot intermediate band solar cell. Paper presented at the 37th photovoltaic specialists conference, Seattle, pp 001907–12

12. Linares PG, Marti A, Antolin E, Luque A (2011) III-V compound semiconductor screening for implementing quantum dot intermediate band solar cells. J Appl Phys 109:014313
13. Popescu V, Bester G, Hanna MC, Norman AG, Zunger A (2008) Theoretical and experimental examination of the intermediate-band concept for strain-balanced (In,Ga)As/Ga(As,P) quantum dot solar cells. Phys Rev B 78:205321
14. Lazarenkova OL, Balandin AA (2001) Miniband formation in a quantum dot crystal. J Appl Phys 89(10):5509–5515
15. Shao Q, Balandin AA, Fedoseyev AI, Turowski M (2007) Intermediate-band solar cells based on quantum dot supracrystals. Appl Phys Lett 91(16):163503. doi:10.1063/1.2799172
16. Luque A, Marti A, Antolin E, Garcia-Linares P (2010) Intraband absorption for normal illumination in quantum dot intermediate band solar cells. Sol Energy Mater Sol Cells 94:2032–2035
17. Luque A, Marti A, Mellor A, Marron DF, Tobias I, Antolín E (2013) Absorption coefficient for the intraband transitions in quantum dot materials. Prog Photovoltaics 21:658–667. doi:10.1002/pip.1250
18. Luque A, Mellor A, Tobías I, Antolín E, Linares PG, Ramiro I, Martí A (2013) Virtual-bound, filamentary and layered states in a box-shaped quantum dot of square potential form the exact numerical solution of the effective mass Schrödinger equation. Phys B 413:73–81. doi:10.1016/j.physb.2012.12.047
19. Bastard G, Ziemelis UO, Delalande C, Voos M, Gossard AC, Wiegmann W (1984) Bound and virtual bound-states in semiconductor quantum wells. Solid State Commun 49(7):671–674
20. Ferreira R, Bastard G (2006) Unbound states in quantum heterostructures. Nanoscale Res Lett 1(2):120–136. doi:10.1007/s11671-006-9000-1
21. Fermi E (1932) Quantum theory of radiation. Rev Mod Phys 4(1):0087–0132
22. Heitler W (1944) The quantum theory of radiation. Oxford University Press, Oxford
23. Berestetski V, Lifchitz E, Pitayevski L (1972) Théorie quantique relativiste. Mir, Moscou
24. Luque A, Marti A, Antolín E, Linares PG, Tobías I, Ramiro I, Hernandez E (2011) New Hamiltonian for a better understanding of the quantum dot intermediate band solar cells. Sol Energy Mater Sol Cells 95:2095–2101. doi:10.1016/j.solmat.2011.02.028
25. Luque A, Marti A, Mellor A, Marron DF, Tobias I, Antolín E (2013) Absorption coefficient for the intraband transitions in quantum dot materials. Prog Photovoltaics 21:658–667. doi:10.1002/pip.1250
26. Luque A, Martí A, Cuadra L (2001) Thermodynamic consistency of sub-bandgap absorbing solar cell proposals. IEEE Trans Electron Devices 48(9):2118–2124
27. Phillips J, Kamath K, Zhou X, Chervela N, Bhattacharya P (1997) Photoluminescence and far-infrared absorption in Si-doped self-organized InAs quantum dots. Appl Phys Lett 71(15):2079–2081. doi:10.1063/1.119347
28. Sauvage S, Boucaud P, Julien FH, Gerard JM, ThierryMieg V (1997) Intraband absorption in n-doped InAs/GaAs quantum dots. Appl Phys Lett 71(19):2785–2787. doi:10.1063/1.120133
29. Durr CS, Warburton RJ, Karrai K, Kotthaus JP, Medeiros-Ribeiro G, Petroff PM (1998) Interband absorption on self-assembled InAs quantum dots. Phys E 2(1–4):23–27. doi:10.1016/s1386-9477(98)00005-8
30. Popescu V, Bester G, Zunger A (2009) Strain-induced localized states within the matrix continuum of self-assembled quantum dots. Appl Phys Lett 95(2):023108. doi:10.1063/1.3159875
31. Pryor C (1998) Eight-band calculations of strained InAs/GaAs quantum dots compared with one-, four-, and six-band approximations. Phys Rev B 57(12):7190–7195
32. Kato T (1959) Growth properties of solutions of the reduced wave equation with a variable coefficient. Commun Pure Appl Math 12:403–425
33. Agmon S (1970) Lower bounds for solutions of the Schrödinger equations. J Anal Math 23:1–25
34. Luque A, Marti A, Stanley C (2012) Understanding intermediate-band solar cells. Nat Photonics 6(3):146–152. doi:10.1038/nphoton.2012.1